Computer Physics Communications 261 (2021) 107769

Contents lists available at ScienceDirect

Computer Physics Communications

journal homepage: www.elsevier.com/locate/cpc

The bi-Lebedev scheme for the Maxwell eigenvalue problem with 3D bi-anisotropic complex media ☆

Xing-Long Lyu [a], Tiexiang Li [a,b,*], Tsung-Ming Huang [c,**], Wen-Wei Lin [d], Heng Tian [d]

[a] School of Mathematics, Southeast University, Nanjing 211189, People's Republic of China
[b] Nanjing Center for Applied Mathematics, Nanjing 211135, People's Republic of China
[c] Department of Mathematics, National Taiwan Normal University, Taipei 116, Taiwan
[d] Department of Applied Mathematics, National Chiao Tung University, Hsinchu 300, Taiwan

ARTICLE INFO

Article history:
Received 30 May 2020
Received in revised form 2 October 2020
Accepted 27 November 2020
Available online 10 December 2020

Keywords:
Maxwell eigenvalue problem
Bi-Lebedev scheme
3D bi-anisotropic complex media
Null-space free method
Fast Fourier transform

ABSTRACT

This paper focuses on studying the eigenstructure of generalized eigenvalue problems (GEPs) arising in the three-dimensional source-free Maxwell equations for bi-anisotropic complex media with a 3-by-3 permittivity tensor $\varepsilon > 0$, a permeability tensor $\mu > 0$, and scalar magnetoelectric coupling constants $\xi = \bar{\zeta} = \imath\gamma$. The bi-Lebedev scheme is appealing because it preserves the symmetry inherent to the Maxwell eigenvalue problem exactly and because full degrees of freedom of electromagnetic fields at each grid point are taken into account in the discretization. The resulting GEP has eigenvalues appearing in quadruples $\{\pm\omega, \pm\bar{\omega}\}$. We consider two main scenarios, where $\gamma < \gamma_*$ and $\gamma > \gamma_*$ with γ_* as a critical value. In the former case, all the eigenvalues are real. In the latter case, the GEP has complex eigenvalues, and we particularly focus on the bifurcation of the eigenstructure of the GEPs. Numerical results demonstrate that the newborn ground state has occurred after $\gamma = \tilde{\gamma} > \gamma_*$, and the associated eigenvector has an exotic phenomenon of localization. Moreover, the Poynting vectors of the newborn eigenvector not only are concentrated in the material but also display exciting patterns.

1. Introduction

Mathematically, the propagations of electromagnetic fields in bi-isotropic and bi-anisotropic media are modeled by the three-dimensional (3D) source-free Maxwell equations in the frequency domain with the constitutive relations

$$\nabla \times \boldsymbol{E}(\boldsymbol{r}) = \imath\omega \boldsymbol{B}(\boldsymbol{r}), \tag{1a}$$

$$\nabla \times \boldsymbol{H}(\boldsymbol{r}) = -\imath\omega \boldsymbol{D}(\boldsymbol{r}), \tag{1b}$$

$$\nabla \cdot \boldsymbol{B}(\boldsymbol{r}) = 0, \quad \nabla \cdot \boldsymbol{D}(\boldsymbol{r}) = 0, \tag{1c}$$

where ω represents the frequency, $\imath = \sqrt{-1}$, $\boldsymbol{E}$ and $\boldsymbol{H} \in \mathbb{C}^3$ are the electric and magnetic fields, respectively, and $\boldsymbol{B}$ and $\boldsymbol{D} \in \mathbb{C}^3$ are the magnetic induction and dielectric displacement, respectively, at position $\boldsymbol{r} = (x, y, z) \in \mathbb{R}^3$. For the linear nondispersive media, $\boldsymbol{B}$ and $\boldsymbol{D}$ satisfy the following constitutive relations

$$\boldsymbol{B}(\boldsymbol{r}) = \mu(\boldsymbol{r})\boldsymbol{H}(\boldsymbol{r}) + \zeta(\boldsymbol{r})\boldsymbol{E}(\boldsymbol{r}), \quad \boldsymbol{D}(\boldsymbol{r}) = \varepsilon(\boldsymbol{r})\boldsymbol{E}(\boldsymbol{r}) + \xi(\boldsymbol{r})\boldsymbol{H}(\boldsymbol{r}), \tag{2}$$

where $\varepsilon(\boldsymbol{r})$ and $\mu(\boldsymbol{r})$ are the permittivity and permeability, respectively, and $\xi(\boldsymbol{r})$, $\zeta(\boldsymbol{r})$ are the magnetoelectric coupling parameters. Here, $\varepsilon(\boldsymbol{r})$, $\mu(\boldsymbol{r})$, $\xi(\boldsymbol{r})$, and $\zeta(\boldsymbol{r})$ are constants in the bi-isotropic media. They are generalized as 3×3 tensors with Hermitian positive definite (HPD) matrices $\varepsilon(\boldsymbol{r})$ and $\mu(\boldsymbol{r})$ for the bi-anisotropic media.

A null-space free method [1,2] is proposed to solve (1) with reciprocal bi-isotropic chiral media, where $\varepsilon(\boldsymbol{r}) > 0$, $\mu(\boldsymbol{r}) = 1$, and

$$\xi(\boldsymbol{r}) = \bar{\zeta}(\boldsymbol{r}) = \begin{cases} \imath\gamma, & \gamma \geq 0, \ \boldsymbol{r} \notin \text{air}, \\ 0, & \text{otherwise}. \end{cases} \tag{3}$$

For $\gamma > \gamma_*$ (a critical value), a novel interesting physical phenomenon indicating that a new ground state is born and the corresponding electromagnetic field is localized in the chiral medium was first found in [2]. In this paper, the interest lies in developing a numerical method to simulate such a new physical phenomenon for the reciprocal bi-anisotropic chiral media with HPD $\varepsilon(\boldsymbol{r})$ and $\mu(\boldsymbol{r})$, and $\xi(\boldsymbol{r})$, $\zeta(\boldsymbol{r})$ in (3).

☆ The review of this paper was arranged by Prof. Hazel Andrew.
* Corresponding author at: School of Mathematics, Southeast University, Nanjing 211189, People's Republic of China.
** Corresponding author.
E-mail addresses: lxl_math@seu.edu.cn (X.-L. Lyu), txli@seu.edu.cn (T. Li), min@ntnu.edu.tw (T.-M. Huang), wwlin@math.nctu.edu.tw (W.-W. Lin), tianheng519@gmail.com (H. Tian).

https://doi.org/10.1016/j.cpc.2020.107769
0010-4655/

The combination of (1a), (2) and (1b) leads to the Maxwell eigenvalue problem (MEP)

$$\begin{bmatrix} 0 & -\nabla\times \\ \nabla\times & 0 \end{bmatrix}\begin{bmatrix} \boldsymbol{E} \\ \boldsymbol{H} \end{bmatrix} = \imath\omega \begin{bmatrix} \varepsilon & \xi \\ \zeta & \mu \end{bmatrix}\begin{bmatrix} \boldsymbol{E} \\ \boldsymbol{H} \end{bmatrix}. \tag{4}$$

Bloch's theorem [3] requires that the eigenfields $\boldsymbol{E}$ and $\boldsymbol{H}$ of (4) in 3D periodic media with lattice translation vectors $\{\boldsymbol{a}_\ell\}_{\ell=1}^3$ satisfy the quasiperiodic condition

$$\boldsymbol{E}(\boldsymbol{r}+\boldsymbol{a}_\ell) = e^{\imath 2\pi \boldsymbol{k}\cdot\boldsymbol{a}_\ell}\boldsymbol{E}(\boldsymbol{r}),\ \boldsymbol{H}(\boldsymbol{r}+\boldsymbol{a}_\ell) = e^{\imath 2\pi \boldsymbol{k}\cdot\boldsymbol{a}_\ell}\boldsymbol{H}(\boldsymbol{r}),\ \ell = 1, 2, 3, \tag{5}$$

for a Bloch wave vector $\boldsymbol{k}$.

In recent decades, several numerical methods, including plane-wave expansion methods [4,5], finite element methods [6–9], and finite difference (FD) methods [10–14], have been developed to solve the MEP (4); see the references therein for further details. The plane-wave method is widely used to find numerical solutions of Maxwell's equations with periodic or quasiperiodic boundary conditions. The advantage is that the solution can be easily expanded as the superposition of a sequence of plane waves without any preprocessing. The finite element method is a popular choice for the simulation domain with an irregular shape and/or a complicated interior interface. To the best of our knowledge, in this case, the unstructured mesh is indispensable for this method to attain a desired accuracy, and the solution of an unstructured large sparse linear system is necessary and is usually beyond the scope of applications of the commonly used fast Fourier transform (FFT).

In 1966, a special FD method called Yee's scheme [14] was developed that is attractive for simulating isotropic photonic crystals (*i.e.*, without magnetoelectric coupling), owing to its simplicity and preservation of physical properties by which (4) can be conveniently discretized into a generalized eigenvalue problem (GEP). For 3D anisotropic photonic crystals, some researchers have proposed the Lebedev scheme [15–17] by which (1a) and (1b) are discretized on the Lebedev grid. A Lebedev grid can be seen as a superposition of the standard Yee grid and three shifted Yee grids, as illustrated in Fig. 1.

This paper introduces the bi-Lebedev scheme [18,19] to solve the MEP (4) with 3D reciprocal bi-anisotropic complex media. The so-called bi-Lebedev scheme artificially introduces another copy of the Lebedev grid that coincides with the one shown in Fig. 1(a) but with the color exchanged (red $\to$ blue, blue $\to$ red). Consequently, the same Lebedev scheme can be used to discretize (1a) and (1b) separately on these two replicas of the Lebedev grid with two different sets of variables, $\{\boldsymbol{E}$(red), $\boldsymbol{H}$(blue), $\boldsymbol{D}$(red), $\boldsymbol{B}$(blue)$\}$ and $\{\boldsymbol{E}$(blue), $\boldsymbol{H}$(red), $\boldsymbol{D}$(blue), $\boldsymbol{B}$(red)$\}$, which are coupled with each other only when the bi-anisotropic constitutive relations (2) are evaluated [18,19].

In this paper, we make the following contributions to solving the MEP (4) with 3D bi-anisotropic complex media.

- Using the bi-Lebedev scheme, we provide a detailed FD discretization of the MEP (4) together with the quasiperiodic condition (5) with 3D bi-anisotropic complex media to produce a GEP. The matrices of the discrete permittivity ε and permeability μ preserve the HPD property if ε and μ are HPD. With $\xi = \bar{\zeta} \in \mathbb{C}$ in (3), eigenvalues of the resulting GEP appear as the pair $\{\omega, -\omega\}$ if $\omega \in \mathbb{R} \cup \imath\mathbb{R}$, and they appear the quadruplet $\{\omega, -\omega, \bar{\omega}, -\bar{\omega}\}$ if $\omega \in \mathbb{C}\backslash(\mathbb{R} \cup \imath\mathbb{R})$. Moreover, by applying singular value decomposition (SVD) of the discrete single-curl operator, we develop a null-space free method to solve the resulting GEP.
- We adopt a 3-by-3 permittivity HPD matrix ε and the permeability $\mu = I_3$ and take $\xi = \bar{\zeta}$ in (3) with $\gamma > \gamma_* \approx 1.204$ to make the weight matrix $\begin{bmatrix} \varepsilon & \xi \\ \zeta & \mu \end{bmatrix}$ indefinite, which results in extremely complicated eigenstructures of the discrete MEP (4). Here, the weight matrix is HPD if $\gamma < \gamma_*$ and singular if $\gamma = \gamma_*$ (a critical value). With a similar derivation in Section 3 of [2], the discrete MEP (4) has real eigenvalues $\pm\omega$ for $\gamma < \gamma_*$ and abundant 2×2 Jordan blocks at $\omega = \infty$ when $\gamma = \gamma_*$. For $\gamma > \gamma_*$, a mass of eigenvalue tetrads $(\omega, -\omega, \bar{\omega}, -\bar{\omega})$ with $|\mathrm{Re}(\omega)| \approx 0$ and $|\mathrm{Im}(\omega)| \gg 0$ are created, some of which collide rapidly near the origin and then bifurcate into positive and negative real eigenvalues, respectively. The newborn positive eigenvalue pushes the original eigenvalues farther from zero, *i.e.*, the newborn eigenstate possesses less energy (frequency) than that of the original ground state. Moreover, the associated eigenfields are highly confined in the bi-anisotropic chiral medium with negligible leakage to the outside.
- By virtue of the bi-Lebedev scheme, the eigenvectors of the discrete MEP (4) provide complete components of both $\boldsymbol{E}(\boldsymbol{r})$ and $\boldsymbol{H}(\boldsymbol{r})$ at each grid point; therefore, the Poynting vector $\boldsymbol{S} = \frac{1}{2}\Re(\boldsymbol{E} \times \bar{\boldsymbol{H}})$ is instantly accessible at any grid point without any additional approximations once the eigenvector is given. In this work, we demonstrate that the Poynting vector associated with the newborn eigenvalue is also concentrated in the reciprocal bi-anisotropic chiral medium. More interestingly, the spatial distribution of Poynting vectors inside the chiral medium displays some peculiar patterns.

This paper is outlined as follows. In Section 2, we define the notations of the discrete $\boldsymbol{E}(\boldsymbol{r})$, $\boldsymbol{H}(\boldsymbol{r})$, $\varepsilon(\boldsymbol{r})$, $\mu(\boldsymbol{r})$, $\xi(\boldsymbol{r})$ and $\zeta(\boldsymbol{r})$ on a Lebedev grid. In Section 3, we provide the detailed matrix representation of bi-Lebedev scheme from which the MEP (4) is discretized into a sparse GEP of enormous dimension. The SVD of the discrete single-curl operator in this scheme and a null-space free method for the GEP are derived in Section 4. Numerical results are provided in Section 5 to show the colliding eigenvalues and localization of eigenfields and Poynting vectors. Finally, concluding remarks are given in Section 6.

Notations. Bold letters denote vectors; $I_n = [\mathbf{e}_1, \mathbf{e}_2, \ldots, \mathbf{e}_n]$ is the identity matrix of size n. For matrices A and B, $A^\top$ and A^* are the transpose and conjugate transpose, respectively; $A \otimes B$ and $A \oplus B = \mathrm{diag}(A, B)$ are the Kronecker product and the direct sum of A and B, respectively; $\mathrm{vec}(A)$ is the vectorization function of the matrix A.

2. Discretization of $\boldsymbol{E}, \boldsymbol{H}, \boldsymbol{\varepsilon}, \boldsymbol{\mu}, \boldsymbol{\xi}, \boldsymbol{\zeta}$ on the Lebedev grid

First, it is worth noting that in this and the next two sections, $\xi(\boldsymbol{r})$ and $\zeta(\boldsymbol{r})^*$ can be any 3-by-3 complex matrices.

Crystal structures can be classified as 14 Bravais lattices in 3D Euclidean space [20]. In fact, a primitive cell of a Bravais lattice, which is a parallelepiped formed by the lattice translation vectors $\{\boldsymbol{a}_\ell\}_{\ell=1}^3$, can be embedded into a minimally contained rectangular cuboid called the working cell Ω_c. Let the working cell be partitioned evenly by n_1, n_2 and n_3 grid points in the x-, y-, and z-direction, respectively, and δ_x, δ_y and δ_z be the corresponding mesh lengths. For simplicity, we introduce the shorthand notations $(r, s, t) \equiv (r\delta_x, s\delta_y, t\delta_z)$, where $r, s, t \in \mathbb{R}$, and $\hat{\imath} \equiv i + \frac{1}{2}, \hat{\jmath} \equiv j + \frac{1}{2}, \hat{k} \equiv k + \frac{1}{2}$ for $i = 0, 1, \ldots, n_1 - 1$, $j = 0, 1, \ldots, n_2 - 1$, and $k = 0, 1, \ldots, n_3 - 1$.

As mentioned in Section 1, the components of $\boldsymbol{E}(\boldsymbol{r})$ and $\boldsymbol{H}(\boldsymbol{r})$ attached to the Lebedev grid naturally form four groups shown in Fig. 1. Specifically, as shown in Fig. 1(b), the components of $\boldsymbol{E}(\boldsymbol{r})$ and $\boldsymbol{H}(\boldsymbol{r})$ on the standard Yee grid can be represented by

$$E_1(\hat{\imath}, j, k),\ E_2(i, \hat{\jmath}, k),\ E_3(i, j, \hat{k}), \tag{6a}$$

$$H_1(i, \hat{\jmath}, \hat{k}),\ H_2(\hat{\imath}, j, \hat{k}),\ H_3(\hat{\imath}, \hat{\jmath}, k), \tag{6b}$$

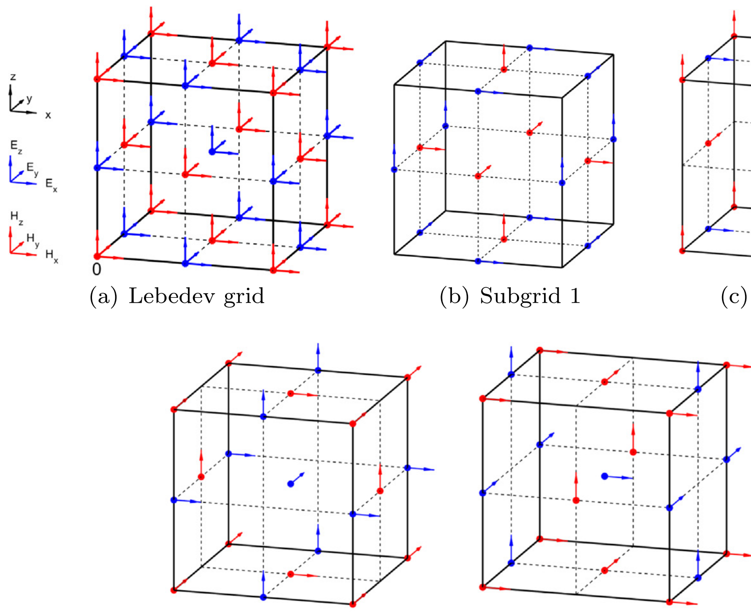

(a) Lebedev grid (b) Subgrid 1 (c) Subgrid 2

(d) Subgrid 3 (e) Subgrid 4

Fig. 1. (a) Illustration of the Lebedev grid and the collocated $\boldsymbol{E}$ and $\boldsymbol{H}$ components. (b) Standard Yee grid. (c) Yee grid shifted by $(\pm\frac{\delta_x}{2}, \pm\frac{\delta_y}{2}, 0)$. (d) Yee grid shifted by $(\pm\frac{\delta_x}{2}, 0, \pm\frac{\delta_z}{2})$. (e) Yee grid shifted by $(0, \pm\frac{\delta_y}{2}, \pm\frac{\delta_z}{2})$. (For interpretation of the references to color in this figure legend, the reader is referred to the web version of this article.)

respectively. Next, as shown in Fig. 1(c), we shift the components of $\boldsymbol{E}(\boldsymbol{r})$ and $\boldsymbol{H}(\boldsymbol{r})$ in (6) by $(\pm\frac{\delta_x}{2}, \pm\frac{\delta_y}{2}, 0)$, yielding

$$E_1(i, \hat{j}, k),\ E_2(\hat{i}, j, k),\ E_3(\hat{i}, \hat{j}, \hat{k}),$$
$$H_1(\hat{i}, j, \hat{k}),\ H_2(i, \hat{j}, \hat{k}),\ H_3(i, j, k).$$

Then, as shown in Fig. 1(d), we shift the components of $\boldsymbol{E}(\boldsymbol{r})$ and $\boldsymbol{H}(\boldsymbol{r})$ in (6) by $(\pm\frac{\delta_x}{2}, 0, \pm\frac{\delta_z}{2})$, yielding

$$E_1(i, j, \hat{k}),\ E_2(\hat{i}, \hat{j}, \hat{k}),\ E_3(\hat{i}, j, k),$$
$$H_1(\hat{i}, \hat{j}, k),\ H_2(i, j, k),\ H_3(i, \hat{j}, \hat{k}).$$

Last, as shown in Fig. 1(e), we shift the components of $\boldsymbol{E}(\boldsymbol{r})$ and $\boldsymbol{H}(\boldsymbol{r})$ in (6) by $(0, \pm\frac{\delta_y}{2}, \pm\frac{\delta_z}{2})$, yielding

$$E_1(\hat{i}, \hat{j}, \hat{k}),\ E_2(i, j, \hat{k}),\ E_3(i, \hat{j}, k),$$
$$H_1(i, j, k),\ H_2(\hat{i}, \hat{j}, k),\ H_3(\hat{i}, j, \hat{k}).$$

Furthermore, we collect these four groups of the components of $\boldsymbol{E}(\boldsymbol{r})$ into four column vectors $\mathbf{e}_{e1}, \mathbf{e}_{e2}, \mathbf{e}_{e3}$ and $\mathbf{e}_{e4}$, and the four groups of components of $\boldsymbol{H}(\boldsymbol{r})$ into four column vectors $\mathbf{h}_{f1}, \mathbf{h}_{f2}, \mathbf{h}_{f3}$ and $\mathbf{h}_{f4}$. By defining $\check{F}(:,:,:) \equiv \text{vec}(F(:,:,:))$, where $F(:,:,:)$ is a three-way array, these vectors can be defined as follows:

$$\mathbf{e}_{e1} = \begin{bmatrix} \check{E}_1(\hat{0}:\hat{n}_1-1, 0:n_2-1, 0:n_3-1) \\ \check{E}_2(0:n_1-1, \hat{0}:\hat{n}_2-1, 0:n_3-1) \\ \check{E}_3(0:n_1-1, 0:n_2-1, \hat{0}:\hat{n}_3-1) \end{bmatrix},$$

$$\mathbf{h}_{f1} = \begin{bmatrix} \check{H}_1(0:n_1-1, \hat{0}:\hat{n}_2-1, \hat{0}:\hat{n}_3-1) \\ \check{H}_2(\hat{0}:\hat{n}_1-1, 0:n_2-1, \hat{0}:\hat{n}_3-1) \\ \check{H}_3(\hat{0}:\hat{n}_1-1, \hat{0}:\hat{n}_2-1, 0:n_3-1) \end{bmatrix}, \tag{7a}$$

$$\mathbf{e}_{e2} = \begin{bmatrix} \check{E}_1(0:n_1-1, \hat{0}:\hat{n}_2-1, 0:n_3-1) \\ \check{E}_2(\hat{0}:\hat{n}_1-1, 0:n_2-1, 0:n_3-1) \\ \check{E}_3(\hat{0}:\hat{n}_1-1, \hat{0}:\hat{n}_2-1, \hat{0}:\hat{n}_3-1) \end{bmatrix},$$

$$\mathbf{h}_{f2} = \begin{bmatrix} \check{H}_1(\hat{0}:\hat{n}_1-1, 0:n_2-1, \hat{0}:\hat{n}_3-1) \\ \check{H}_2(0:n_1-1, \hat{0}:\hat{n}_2-1, \hat{0}:\hat{n}_3-1) \\ \check{H}_3(0:n_1-1, 0:n_2-1, 0:n_3-1) \end{bmatrix}, \tag{7b}$$

$$\mathbf{e}_{e3} = \begin{bmatrix} \check{E}_1(0:n_1-1, 0:n_2-1, \hat{0}:\hat{n}_3-1) \\ \check{E}_2(\hat{0}:\hat{n}_1-1, \hat{0}:\hat{n}_2-1, \hat{0}:\hat{n}_3-1) \\ \check{E}_3(\hat{0}:\hat{n}_1-1, 0:n_2-1, 0:n_3-1) \end{bmatrix},$$

$$\mathbf{h}_{f3} = \begin{bmatrix} \check{H}_1(\hat{0}:\hat{n}_1-1, \hat{0}:\hat{n}_2-1, 0:n_3-1) \\ \check{H}_2(0:n_1-1, 0:n_2-1, 0:n_3-1) \\ \check{H}_3(0:n_1-1, \hat{0}:\hat{n}_2-1, \hat{0}:\hat{n}_3-1) \end{bmatrix}, \tag{7c}$$

$$\mathbf{e}_{e4} = \begin{bmatrix} \check{E}_1(\hat{0}:\hat{n}_1-1, \hat{0}:\hat{n}_2-1, \hat{0}:\hat{n}_3-1) \\ \check{E}_2(0:n_1-1, 0:n_2-1, \hat{0}:\hat{n}_3-1) \\ \check{E}_3(0:n_1-1, \hat{0}:\hat{n}_2-1, 0:n_3-1) \end{bmatrix},$$

$$\mathbf{h}_{f4} = \begin{bmatrix} \check{H}_1(0:n_1-1, 0:n_2-1, 0:n_3-1) \\ \check{H}_2(\hat{0}:\hat{n}_1-1, \hat{0}:\hat{n}_2-1, 0:n_3-1) \\ \check{H}_3(\hat{0}:\hat{n}_1-1, 0:n_2-1, \hat{0}:\hat{n}_3-1) \end{bmatrix}. \tag{7d}$$

For convenience, we define

$$\mathbf{e}_e = [\mathbf{e}_{e1}^\top, \mathbf{e}_{e2}^\top, \mathbf{e}_{e3}^\top, \mathbf{e}_{e4}^\top]^\top$$

for $\boldsymbol{E}(\boldsymbol{r})$ sampled at midpoints of edges and centroids, and

$$\mathbf{h}_f = [\mathbf{h}_{f1}^\top, \mathbf{h}_{f2}^\top, \mathbf{h}_{f3}^\top, \mathbf{h}_{f4}^\top]^\top$$

for $\boldsymbol{H}(\boldsymbol{r})$ sampled at face centers and vertices.

In the bi-Lebedev scheme, by just interchanging the symbols $\mathbf{e}$ and $\mathbf{h}$ in (7), we can define

$$\mathbf{e}_f = [\mathbf{e}_{f1}^\top, \mathbf{e}_{f2}^\top, \mathbf{e}_{f3}^\top, \mathbf{e}_{f4}^\top]^\top$$

for $\boldsymbol{E}(\boldsymbol{r})$ sampled at face centers and vertices, and

$$\mathbf{h}_e = [\mathbf{h}_{e1}^\top, \mathbf{h}_{e2}^\top, \mathbf{h}_{e3}^\top, \mathbf{h}_{e4}^\top]^\top$$

for $\boldsymbol{H}(\boldsymbol{r})$ sampled at midpoints of edges and centroids.

Next, we consider the anisotropic permittivity $\varepsilon(\boldsymbol{r})$, permeability $\mu(\boldsymbol{r})$ and magnetoelectric coupling tensors $\xi(\boldsymbol{r})$ and $\zeta(\boldsymbol{r})^*$. For convenience, we let $s = \varepsilon, \mu, \xi, \zeta$ and write $s(\boldsymbol{r}) = [s_{pq}(\boldsymbol{r})]_{p,q=1}^3$. In addition, we define $\mathcal{S}^{(\mathrm{c})}(s)$ for c = e or f as the corresponding assembled weight matrix. The detailed definition can be found in Appendix A.

Theorem 1. *If $s = [s_{pq}(\boldsymbol{r})] \in \mathbb{C}^{3\times 3}$ is HPD, for $s = \varepsilon$ or μ, then $\mathcal{S}^{(\mathrm{c})}(s)$ for c = e or f is also HPD.*

Proof. See Appendix C.1. □

3. Discretization of MEP with 3D Bi-anisotropic complex media

In this section, we present the detailed discretization of the MEP (4) using the bi-Lebedev scheme. To simplify the notation of the discrete single-curl operator, we define a function $\mathcal{C}(X_1, X_2, X_3)$ as

$$\mathcal{C}(X_1, X_2, X_3) = \begin{bmatrix} 0 & -X_3 & X_2 \\ X_3 & 0 & -X_1 \\ -X_2 & X_1 & 0 \end{bmatrix},$$

where X_1, X_2 and X_3 are three square matrices of the same size. Without loss of generality, hereafter, we take the face-centered cubic (FCC) lattice as an example. The discrete single-curl operator with the quasiperiodic condition (5) using Yee's scheme can be represented by the matrix $\mathcal{C}(C_1, C_2, C_3)$ [1,12], where

$$C_1 = \frac{1}{\delta_x} I_{n_2 n_3} \otimes K_{1,n_1}(e^{\imath \hat{\boldsymbol{k}}\cdot \boldsymbol{a}_1}),\ K_{m_1,m_2}(X) = \begin{bmatrix} 0 & I_{m_1(m_2-1)} \\ X & 0 \end{bmatrix} - I_{m_1 m_2}, \tag{8a}$$

$$C_2 = \frac{1}{\delta_y} I_{n_3} \otimes K_{n_1,n_2}(e^{\imath \hat{\boldsymbol{k}}\cdot \boldsymbol{a}_2} J_1),\quad J_1 = \begin{bmatrix} 0 & e^{-\imath \hat{\boldsymbol{k}}\cdot \boldsymbol{a}_1} I_{n_1/2} \\ I_{n_1/2} & 0 \end{bmatrix}, \tag{8b}$$

$$C_3 = \frac{1}{\delta_z} K_{n_1 n_2, n_3}(e^{\imath \hat{\boldsymbol{k}}\cdot \boldsymbol{a}_3} J_2),\quad J_2 = \begin{bmatrix} 0 & e^{-\imath \hat{\boldsymbol{k}}\cdot \boldsymbol{a}_2} I_{n_2/3} \otimes I_{n_1} \\ I_{2n_2/3} \otimes J_1 & 0 \end{bmatrix}, \tag{8c}$$

with $\hat{\boldsymbol{k}} = 2\pi \boldsymbol{k}$. In passing, the most general expressions of C_1, C_2 and C_3 for any Bravais lattice corresponding to (8) can be found in [21].

3.1. Matrix representation of $\nabla \times \boldsymbol{E} = \imath\omega \boldsymbol{B}$ at face centers

In this subsection, we derive the matrix representations of the FD discretization of (1a) on subgrids 1, 2, 3 and 4 illustrated in Figs. 1(b), 1(c), 1(d), and 1(e), respectively. Specifically, we first write down the central FD approximation of (1a) in the componentwise form at each grid point and then recast all formulas for each subgrid into matrix–vector form. The detailed explanation can be found in Appendix B. Moreover, the details of how to incorporate the quasiperiodic condition (5) into the FD formula, which have been thoroughly discussed in [21] for the Yee grid (*i.e.*, subgrid 1), hold for subgrids 2,3 and 4.

Denote $\mathcal{Z}_{pq}^{(\mathrm{f})}(\cdot) = \mathcal{S}_{pq}^{(\mathrm{f})}(\cdot, \zeta)$ and $\mathcal{M}_{pq}^{(\mathrm{f})}(\cdot) = \mathcal{S}_{pq}^{(\mathrm{f})}(\cdot, \mu)$, which are defined in (A.1) in Appendix A. Using the FD discretization of (1a) at

- $(i, \hat{j}, \hat{k})$, $(\hat{i}, j, \hat{k})$ and $(\hat{i}, \hat{j}, k)$, respectively, in Subgrid 1 (Fig. 1(b));
- $(\hat{i}, j, \hat{k})$, $(i, \hat{j}, \hat{k})$ and (i, j, k), respectively, in Subgrid 2 (Fig. 1(c));
- $(\hat{i}, \hat{j}, k)$, (i, j, k) and $(i, \hat{j}, \hat{k})$, respectively, in Subgrid 3 (Fig. 1(d));
- (i, j, k), $(\hat{i}, \hat{j}, k)$ and $(\hat{i}, j, \hat{k})$, respectively, in Subgrid 4 (Fig. 1(e)),

the resulting matrix representations are

$$\begin{aligned} &\mathcal{C}(C_1, C_2, C_3)\mathbf{e}_{e1} \\ &= \imath\omega\Big(\begin{bmatrix} \mathcal{Z}_{11}^{(\mathrm{f})} & \mathcal{Z}_{12}^{(\mathrm{f})} & \mathcal{Z}_{13}^{(\mathrm{f})} & \mathcal{Z}_{14}^{(\mathrm{f})} \end{bmatrix}\mathbf{e}_f \\ &\quad + \begin{bmatrix} \mathcal{M}_{11}^{(\mathrm{f})} & \mathcal{M}_{12}^{(\mathrm{f})} & \mathcal{M}_{13}^{(\mathrm{f})} & \mathcal{M}_{14}^{(\mathrm{f})} \end{bmatrix}\mathbf{h}_f\Big), \end{aligned} \tag{9a}$$

$$\begin{aligned} &\mathcal{C}(-C_1^*, -C_2^*, C_3)\mathbf{e}_{e2} \\ &= \imath\omega\Big(\begin{bmatrix} \mathcal{Z}_{21}^{(\mathrm{f})} & \mathcal{Z}_{22}^{(\mathrm{f})} & \mathcal{Z}_{23}^{(\mathrm{f})} & \mathcal{Z}_{24}^{(\mathrm{f})} \end{bmatrix}\mathbf{e}_f \\ &\quad + \begin{bmatrix} \mathcal{M}_{21}^{(\mathrm{f})} & \mathcal{M}_{22}^{(\mathrm{f})} & \mathcal{M}_{23}^{(\mathrm{f})} & \mathcal{M}_{24}^{(\mathrm{f})} \end{bmatrix}\mathbf{h}_f\Big), \end{aligned} \tag{9b}$$

$$\begin{aligned} &\mathcal{C}(-C_1^*, C_2, -C_3^*)\mathbf{e}_{e3} \\ &= \imath\omega\Big(\begin{bmatrix} \mathcal{Z}_{31}^{(\mathrm{f})} & \mathcal{Z}_{32}^{(\mathrm{f})} & \mathcal{Z}_{33}^{(\mathrm{f})} & \mathcal{Z}_{34}^{(\mathrm{f})} \end{bmatrix}\mathbf{e}_f \\ &\quad + \begin{bmatrix} \mathcal{M}_{31}^{(\mathrm{f})} & \mathcal{M}_{32}^{(\mathrm{f})} & \mathcal{M}_{33}^{(\mathrm{f})} & \mathcal{M}_{34}^{(\mathrm{f})} \end{bmatrix}\mathbf{h}_f\Big), \end{aligned} \tag{9c}$$

$$\begin{aligned} &\mathcal{C}(C_1, -C_2^*, -C_3^*)\mathbf{e}_{e4} \\ &= \imath\omega\Big(\begin{bmatrix} \mathcal{Z}_{41}^{(\mathrm{f})} & \mathcal{Z}_{42}^{(\mathrm{f})} & \mathcal{Z}_{43}^{(\mathrm{f})} & \mathcal{Z}_{44}^{(\mathrm{f})} \end{bmatrix}\mathbf{e}_f \\ &\quad + \begin{bmatrix} \mathcal{M}_{41}^{(\mathrm{f})} & \mathcal{M}_{42}^{(\mathrm{f})} & \mathcal{M}_{43}^{(\mathrm{f})} & \mathcal{M}_{44}^{(\mathrm{f})} \end{bmatrix}\mathbf{h}_f\Big), \end{aligned} \tag{9d}$$

respectively. The detailed derivation of (9a) is introduced in Appendix B.1; (9b), (9c) and (9d) can be obtained similarly. From (9), (1a) is discretized at face centers and vertices into

$$\tilde{\mathcal{C}}\mathbf{e}_e = \imath\omega\left(\mathcal{Z}_{(\mathrm{f})}\mathbf{e}_f + \mathcal{M}_{(\mathrm{f})}\mathbf{h}_f\right), \tag{10a}$$

where

$$\begin{aligned} \tilde{\mathcal{C}} = \mathrm{diag}\big(&\mathcal{C}(C_1, C_2, C_3), \mathcal{C}(-C_1^*, -C_2^*, C_3), \mathcal{C}(-C_1^*, C_2, -C_3^*), \\ &\mathcal{C}(C_1, -C_2^*, -C_3^*)\big). \end{aligned} \tag{10b}$$

3.2. Matrix representation of $\nabla \times \boldsymbol{E} = \imath\omega \boldsymbol{B}$ at midpoints of edges

In this subsection, we discretize (1b) on subgrids 1, 2, 3 and 4 illustrated in Figs. 1(b), 1(c), 1(d), and 1(e), respectively. Similarly, we recast all formulas for each subgrid into matrix–vector form.

Using the FD discretization for (1a) at

- $(\hat{i}, j, k)$, $(i, \hat{j}, k)$, and $(i, j, \hat{k})$, respectively, in Subgrid 1 (Fig. 1(b));
- $(i, \hat{j}, k)$, $(\hat{i}, j, k)$ and $(\hat{i}, \hat{j}, \hat{k})$, respectively, in Subgrid 2 (Fig. 1(c));
- $(i, j, \hat{k})$, $(\hat{i}, \hat{j}, \hat{k})$ and $(\hat{i}, j, k)$, respectively, in Subgrid 3 (Fig. 1(d));
- $(\hat{i}, \hat{j}, \hat{k})$, $(i, j, \hat{k})$ and $(i, \hat{j}, k)$, respectively, in Subgrid 4 (Fig. 1(e)),

the resulting matrix representations are

$$\begin{aligned} &\mathcal{C}(C_1, C_2, C_3)^*\mathbf{e}_{f1} \\ &= \imath\omega\left(\begin{bmatrix} \mathcal{Z}_{11}^{(\mathrm{e})} & \mathcal{Z}_{12}^{(\mathrm{e})} & \mathcal{Z}_{13}^{(\mathrm{e})} & \mathcal{Z}_{14}^{(\mathrm{e})} \end{bmatrix}\mathbf{e}_e \right.\\ &\quad \left. + \begin{bmatrix} \mathcal{M}_{11}^{(\mathrm{e})} & \mathcal{M}_{12}^{(\mathrm{e})} & \mathcal{M}_{13}^{(\mathrm{e})} & \mathcal{M}_{14}^{(\mathrm{e})} \end{bmatrix}\mathbf{h}_e\right), \end{aligned} \tag{11a}$$

$$\begin{aligned} &\mathcal{C}(-C_1^*, -C_2^*, C_3)^*\mathbf{e}_{f2} \\ &= \imath\omega\left(\begin{bmatrix} \mathcal{Z}_{21}^{(\mathrm{e})} & \mathcal{Z}_{22}^{(\mathrm{e})} & \mathcal{Z}_{23}^{(\mathrm{e})} & \mathcal{Z}_{24}^{(\mathrm{e})} \end{bmatrix}\mathbf{e}_e \right.\\ &\quad \left. + \begin{bmatrix} \mathcal{M}_{21}^{(\mathrm{e})} & \mathcal{M}_{22}^{(\mathrm{e})} & \mathcal{M}_{23}^{(\mathrm{e})} & \mathcal{M}_{24}^{(\mathrm{e})} \end{bmatrix}\mathbf{h}_e\right), \end{aligned} \tag{11b}$$

$$\begin{aligned} &\mathcal{C}(-C_1^*, C_2, -C_3^*)^*\mathbf{e}_{f3} \\ &= \imath\omega\left(\begin{bmatrix} \mathcal{Z}_{31}^{(\mathrm{e})} & \mathcal{Z}_{32}^{(\mathrm{e})} & \mathcal{Z}_{33}^{(\mathrm{e})} & \mathcal{Z}_{34}^{(\mathrm{e})} \end{bmatrix}\mathbf{e}_e \right.\\ &\quad \left. + \begin{bmatrix} \mathcal{M}_{31}^{(\mathrm{e})} & \mathcal{M}_{32}^{(\mathrm{e})} & \mathcal{M}_{33}^{(\mathrm{e})} & \mathcal{M}_{34}^{(\mathrm{e})} \end{bmatrix}\mathbf{h}_e\right), \end{aligned} \tag{11c}$$

$\mathcal{C}(C_1, -C_2^*, -C_3^*)^*\mathbf{e}_{f4}$

$$= \imath\omega\left(\begin{bmatrix}\mathcal{Z}_{41}^{(\mathrm{e})} & \mathcal{Z}_{42}^{(\mathrm{e})} & \mathcal{Z}_{43}^{(\mathrm{e})} & \mathcal{Z}_{44}^{(\mathrm{e})}\end{bmatrix}\mathbf{e}_e + \begin{bmatrix}\mathcal{M}_{41}^{(\mathrm{e})} & \mathcal{M}_{42}^{(\mathrm{e})} & \mathcal{M}_{43}^{(\mathrm{e})} & \mathcal{M}_{44}^{(\mathrm{e})}\end{bmatrix}\mathbf{h}_e\right), \tag{11d}$$

respectively. In summary, from (11), (1a) is discretized at midpoints of edges into

$$\tilde{\mathcal{C}}^*\mathbf{e}_f = \imath\omega\left(\mathcal{Z}_{(\mathrm{e})}\mathbf{e}_e + \mathcal{M}_{(\mathrm{e})}\mathbf{h}_e\right), \tag{12}$$

where $\tilde{\mathcal{C}}$ is defined in (10b).

3.3. Matrix representation of $\nabla\times\boldsymbol{H} = -\imath\omega\boldsymbol{D}$ at midpoints of edges

Discretization of (1b) at the midpoints of edges and face centers is a verbatim repetition of the derivations in Sections 3.1 and 3.2 , except that $\boldsymbol{E}(\boldsymbol{r})$ and $\boldsymbol{B}(\boldsymbol{r})$ are replaced with $\boldsymbol{H}(\boldsymbol{r})$ and $\boldsymbol{D}(\boldsymbol{r})$, respectively, and ω is replaced with $-\omega$. The detailed derivations of Section 3.3 are located in Appendix B.2 and those of Section 3.4 in Appendix B.3.

From (B.3a), (B.3b), (B.3c) and (B.3d) in Appendix B.2, the discretization of (1b) at midpoints of edges can be represented as

$$\tilde{\mathcal{C}}^*\mathbf{h}_f = -\imath\omega\left(\mathcal{E}_{(\mathrm{e})}\mathbf{e}_e + \mathcal{X}_{(\mathrm{e})}\mathbf{h}_e\right). \tag{13}$$

3.4. Matrix representation of $\nabla\times\boldsymbol{H} = -\imath\omega\boldsymbol{D}$ at face centers

From (B.4a), (B.4b), (B.4c) and (B.4d) in Appendix B.3, the discretization of (1b) at face centers can be represented as

$$\tilde{\mathcal{C}}\mathbf{h}_e = -\imath\omega\left(\mathcal{E}_{(\mathrm{f})}\mathbf{e}_f + \mathcal{X}_{(\mathrm{f})}\mathbf{h}_f\right). \tag{14}$$

Finally, from (10a), (12), (13) and (14), the MEP (4) is discretized into the following GEP

$$\left[\begin{array}{cc|cc} 0 & 0 & -\tilde{\mathcal{C}}^* & 0\\ 0 & 0 & 0 & -\tilde{\mathcal{C}}\\ \hline \tilde{\mathcal{C}} & 0 & 0 & 0\\ 0 & \tilde{\mathcal{C}}^* & 0 & 0\end{array}\right]\begin{bmatrix}\mathbf{e}_e\\ \mathbf{e}_f\\ \mathbf{h}_f\\ \mathbf{h}_e\end{bmatrix} = \imath\omega\left[\begin{array}{cc|cc} \mathcal{E}_{(\mathrm{e})} & 0 & 0 & \mathcal{X}_{(\mathrm{e})}\\ 0 & \mathcal{E}_{(\mathrm{f})} & \mathcal{X}_{(\mathrm{f})} & 0\\ \hline 0 & \mathcal{Z}_{(\mathrm{f})} & \mathcal{M}_{(\mathrm{f})} & 0\\ \mathcal{Z}_{(\mathrm{e})} & 0 & 0 & \mathcal{M}_{(\mathrm{e})}\end{array}\right]\begin{bmatrix}\mathbf{e}_e\\ \mathbf{e}_f\\ \mathbf{h}_f\\ \mathbf{h}_e\end{bmatrix} \equiv \imath\omega\begin{bmatrix}\mathcal{E} & \mathcal{X}\\ \mathcal{Z} & \mathcal{M}\end{bmatrix}\begin{bmatrix}\mathbf{e}_e\\ \mathbf{e}_f\\ \mathbf{h}_f\\ \mathbf{h}_e\end{bmatrix}. \tag{15}$$

Assume $\xi(\boldsymbol{r}) = \zeta(\boldsymbol{r})^*$. In GEP (15), $\mathcal{E}$ and $\mathcal{M}$ are Hermitian and $\mathcal{X} = \mathcal{Z}^*$. Thus, it is easily seen that (15) is a skew-Hermitian/skew-Hermitian pencil; then, it becomes self-evident that ω and $\bar{\omega}$ are both eigenvalues of the GEP (15). Furthermore, if $(\omega, [\mathbf{e}_e^\top, \mathbf{e}_f^\top, \mathbf{h}_f^\top, \mathbf{h}_e^\top]^\top)$ is an eigenpair of (15), then it is easily seen that $(-\omega, [-\mathbf{e}_e^\top, \mathbf{e}_f^\top, \mathbf{h}_f^\top, -\mathbf{h}_e^\top]^\top)$ is also an eigenpair of (15). In light of these properties, we have the following theorem.

Theorem 2. *Eigenvalues of the GEP (15) appear as the pair $\{\omega, -\omega\}$ if $\omega \in \mathbb{R}\cup\imath\mathbb{R}$, and they appear as the quadruplet $\{\omega, -\omega, \bar{\omega}, -\bar{\omega}\}$ if $\omega \in \mathbb{C}\backslash(\mathbb{R}\cup\imath\mathbb{R})$.*

4. SVD and the fast Eigensolver

Based on the exquisite skills developed in [1,2], we derive the SVD of $\tilde{\mathcal{C}}$ in (10b) and propose a fast eigensolver for the GEP (15).

Theorem 3 ([1,11]). *Let C_ℓ, $\ell = 1, 2, 3$ be defined in (8). Then they are simultaneously diagonalized by the unitary matrix $T \in \mathbb{C}^{n\times n}$, i.e.,*

$$C_\ell T = T\Lambda_\ell, \quad \ell = 1, 2, 3, \tag{16}$$

where Λ_ℓ is the eigenvalue matrix for C_ℓ. The detailed expressions of T and Λ_ℓ can be found in [11,21].

From (16), $\mathcal{C}(C_1, C_2, C_3)$, $\mathcal{C}(-C_1^*, -C_2^*, C_3)$, $\mathcal{C}(-C_1^*, C_2, -C_3^*)$ and $\mathcal{C}(C_1, -C_2^*, -C_3^*)$ in (B.2), (9b), (9c) and (9d), respectively, are equal to

$$(I_3\otimes T)\widetilde{\Lambda}(I_3\otimes T^*), \tag{17}$$

where

$$\widetilde{\Lambda} = \begin{bmatrix} 0 & -\widetilde{\Lambda}_3 & \widetilde{\Lambda}_2\\ \widetilde{\Lambda}_3 & 0 & -\widetilde{\Lambda}_1\\ -\widetilde{\Lambda}_2 & \widetilde{\Lambda}_1 & 0\end{bmatrix}, \tag{18}$$

with $(\widetilde{\Lambda}_1, \widetilde{\Lambda}_2, \widetilde{\Lambda}_3) = (\Lambda_1, \Lambda_2, \Lambda_3)$, $(-\bar{\Lambda}_1, -\bar{\Lambda}_2, \Lambda_3)$, $(-\bar{\Lambda}_1, \Lambda_2, -\bar{\Lambda}_3)$ and $(\Lambda_1, -\bar{\Lambda}_2, -\bar{\Lambda}_3)$, respectively. Let $\widetilde{\Lambda}_\ell = \mathrm{diag}\{\tilde{\lambda}_{1\ell}, \tilde{\lambda}_{2\ell}, \ldots, \tilde{\lambda}_{n\ell}\}$, $\ell = 1, 2, 3$. Doing a perfect shuffle of this $\widetilde{\Lambda}$, *i.e.*, multiplying

$$P = [\mathbf{e}_1, \mathbf{e}_{n+1}, \mathbf{e}_{2n+1}, \mathbf{e}_2, \mathbf{e}_{n+2}, \mathbf{e}_{2n+2}, \ldots, \mathbf{e}_n, \mathbf{e}_{2n}, \mathbf{e}_{3n}] \in \mathbb{R}^{3n\times 3n}$$

and $P^\top$ to $\widetilde{\Lambda}$ from the right and left, respectively, we can transform $\widetilde{\Lambda}$ to a block diagonal matrix

$$P^\top\widetilde{\Lambda}P = L_1\oplus L_2\oplus\cdots\oplus L_n,$$

with

$$L_m = \begin{bmatrix} 0 & -\tilde{\lambda}_{m,3} & \tilde{\lambda}_{m,2}\\ \tilde{\lambda}_{m,3} & 0 & -\tilde{\lambda}_{m,1}\\ -\tilde{\lambda}_{m,2} & \tilde{\lambda}_{m,1} & 0\end{bmatrix}, \quad m = 1, 2, \ldots, n.$$

Theorem 4. *Let $\mathbf{v}_0 \equiv \begin{bmatrix}\ell_1 & \ell_2 & \ell_3\end{bmatrix}^\top$ be a nonzero vector and*

$$L = \begin{bmatrix} 0 & -\ell_3 & \ell_2\\ \ell_3 & 0 & -\ell_1\\ -\ell_2 & \ell_1 & 0\end{bmatrix}. \tag{19}$$

Choose $\alpha, \beta\in\mathbb{R}$ such that $\mathbf{v}_1 \equiv \begin{bmatrix}\beta\bar{\ell}_3 - \bar{\ell}_2 & \bar{\ell}_1 - \alpha\bar{\ell}_3 & \alpha\bar{\ell}_2 - \beta\bar{\ell}_1\end{bmatrix}^\top$ is a nonzero vector. Define $\mathbf{v}_2 = \bar{\mathbf{v}}_0\times\bar{\mathbf{v}}_1$. Then,

$$V \equiv \begin{bmatrix}\frac{\mathbf{v}_0}{\sqrt{\ell_q}} & \frac{\mathbf{v}_1}{\|\mathbf{v}_1\|_2} & \frac{\mathbf{v}_2}{\sqrt{\ell_q}\|\mathbf{v}_1\|_2}\end{bmatrix}, \quad U = \begin{bmatrix}\frac{\bar{\mathbf{v}}_0}{\sqrt{\ell_q}} & \frac{\bar{\mathbf{v}}_2}{\sqrt{\ell_q}\|\mathbf{v}_1\|_2} & -\frac{\bar{\mathbf{v}}_1}{\|\mathbf{v}_1\|_2}\end{bmatrix}$$

are unitary matrices with $\ell_q = |\ell_1|^2 + |\ell_2|^2 + |\ell_3|^2$, and

$$L^*L = V\,\mathrm{diag}\left(0, \ell_q, \ell_q\right)V^*, \quad LL^* = U\,\mathrm{diag}\left(0, \ell_q, \ell_q\right)U^*. \tag{20}$$

Furthermore, L has the following SVD

$$L = U\,\mathrm{diag}\left(0, \sqrt{\ell_q}, \sqrt{\ell_q}\right)V^*. \tag{21}$$

Proof. See Appendix C.2. □

Define

$$\begin{bmatrix}\Psi_0 & \Psi_1 & \Psi_2\end{bmatrix} \equiv \begin{bmatrix}\widetilde{\Lambda}_1 & \Lambda_q - \widetilde{\Lambda}_1\widetilde{\Lambda}_s^* & \widetilde{\Lambda}_3^* - \widetilde{\Lambda}_2^*\\ \widetilde{\Lambda}_2 & \Lambda_q - \widetilde{\Lambda}_2\widetilde{\Lambda}_s^* & \widetilde{\Lambda}_1^* - \widetilde{\Lambda}_3^*\\ \widetilde{\Lambda}_3 & \Lambda_q - \widetilde{\Lambda}_3\widetilde{\Lambda}_s^* & \widetilde{\Lambda}_2^* - \widetilde{\Lambda}_1^*\end{bmatrix}\mathrm{diag}\times\left(\Lambda_q^{-\frac{1}{2}}, \left(3\Lambda_q^2 - \Lambda_q\widetilde{\Lambda}_p\right)^{-\frac{1}{2}}, \left(3\Lambda_q - \widetilde{\Lambda}_p\right)^{-\frac{1}{2}}\right) \tag{22}$$

with

$$\widetilde{\Lambda}_p = \widetilde{\Lambda}_s\widetilde{\Lambda}_s^* \equiv (\widetilde{\Lambda}_1 + \widetilde{\Lambda}_2 + \widetilde{\Lambda}_3)(\widetilde{\Lambda}_1 + \widetilde{\Lambda}_2 + \widetilde{\Lambda}_3)^*,$$
$$\Lambda_q = \Lambda_1^*\Lambda_1 + \Lambda_2^*\Lambda_2 + \Lambda_3^*\Lambda_3.$$

From Theorem 4, we have the SVD of $\widetilde{\Lambda}$ as

$$\widetilde{\Lambda} = \begin{bmatrix}\bar{\Psi}_0 & \bar{\Psi}_1 & -\bar{\Psi}_2\end{bmatrix}\mathrm{diag}(0, \Lambda_q^{1/2}, \Lambda_q^{1/2})\begin{bmatrix}\Psi_0 & \Psi_2 & \Psi_1\end{bmatrix}^*. \tag{23}$$

Denote $\{\Psi_0, \Psi_1, \Psi_2\}$ in (22) by $\{\Psi_{m0}, \Psi_{m1}, \Psi_{m2}\}_{m=1}^4$ for the four cases of $\{\widetilde{\Lambda}_\ell\}_{\ell=1}^3$ as in (18). Substituting (23) into (17), we obtain the SVD of $\mathcal{C}$, as shown in Theorem 5 below.

Theorem 5 (*SVD of $\mathcal{C}$*). *There exist unitary matrices*

$$Q_m \equiv (I_3 \otimes T)\begin{bmatrix}\Psi_{m1} & \Psi_{m2} & \Psi_{m0}\end{bmatrix},$$
$$P_m \equiv (I_3 \otimes T)\begin{bmatrix}-\bar{\Psi}_{m2} & \bar{\Psi}_{m1} & \bar{\Psi}_{m0}\end{bmatrix},$$

for $m = 1, \ldots, 4$, and their first $2n$ columns

$$P_{rm} = (I_3 \otimes T)\begin{bmatrix}-\bar{\Psi}_{m2} & \bar{\Psi}_{m1}\end{bmatrix},\ Q_{rm} = (I_3 \otimes T)\begin{bmatrix}\Psi_{m1} & \Psi_{m2}\end{bmatrix},$$

$m = 1, \ldots, 4,$

such that

$$\mathcal{C}(C_1, C_2, C_3) = P_1\, diag\left(\Lambda_q^{1/2}, \Lambda_q^{1/2}, 0\right) Q_1^* = P_{r1}\widehat{\Sigma}_r Q_{r1}^*,$$
$$\mathcal{C}(-C_1^*, -C_2^*, C_3) = P_2\, diag\left(\Lambda_q^{1/2}, \Lambda_q^{1/2}, 0\right) Q_2^* = P_{r2}\widehat{\Sigma}_r Q_{r2}^*,$$
$$\mathcal{C}(-C_1^*, C_2, -C_3^*) = P_3\, diag\left(\Lambda_q^{1/2}, \Lambda_q^{1/2}, 0\right) Q_3^* = P_{r3}\widehat{\Sigma}_r Q_{r3}^*,$$
$$\mathcal{C}(C_1, -C_2^*, -C_3^*) = P_4\, diag\left(\Lambda_q^{1/2}, \Lambda_q^{1/2}, 0\right) Q_4^* = P_{r4}\widehat{\Sigma}_r Q_{r4}^*,$$

with

$$\widehat{\Sigma}_r = diag\left(\Lambda_q^{1/2}, \Lambda_q^{1/2}\right).$$

Proof. By straightforward verification. □

Let

$$P_r = \operatorname{diag}(P_{r1}, P_{r2}, P_{r3}, P_{r4}),\ Q_r = \operatorname{diag}(Q_{r1}, Q_{r2}, Q_{r3}, Q_{r4}),$$
$$\Sigma_r = I_4 \otimes \widehat{\Sigma}_r.$$

Then, we have

$$\widetilde{\mathcal{C}} = P_r \Sigma_r Q_r^*, \quad \operatorname{diag}(\widetilde{\mathcal{C}}, \widetilde{\mathcal{C}}^*) = \mathcal{P}_r(I_2 \otimes \Sigma_r)\mathcal{Q}_r^*,$$

with

$$\mathcal{P}_r = \operatorname{diag}(P_r, Q_r), \quad \mathcal{Q}_r = \operatorname{diag}(Q_r, P_r).$$

The skew-Hermitian matrix on the left-hand side of (15) has a null space of large dimensions, which would substantially slow the convergence of the desired smallest positive eigenvalues obtained via shift-and-invert-type iterative algorithms. The null-space free technique first developed in [1,11] is used to overcome this drawback and reduce the GEP (15) to the following null-space free GEP (NFGEP) of size $32n \times 32n$:

$$A_r \mathbf{y}_r = \omega\left(\imath\begin{bmatrix}0 & I_2 \otimes \Sigma_r^{-1}\\ -I_2 \otimes \Sigma_r^{-1} & 0\end{bmatrix}\right)\mathbf{y}_r \equiv \omega B_r \mathbf{y}_r, \tag{24a}$$

where

$$A_r \equiv \operatorname{diag}(\mathcal{P}_r^*, \mathcal{Q}_r^*)\begin{bmatrix}\mathcal{M}^{-1}\mathcal{Z} & -I_{24n}\\ I_{24n} & 0\end{bmatrix}\begin{bmatrix}\Phi^{-1} & 0\\ 0 & \mathcal{M}^{-1}\end{bmatrix}$$
$$\times\begin{bmatrix}\mathcal{X}\mathcal{M}^{-1} & I_{24n}\\ -I_{24n} & 0\end{bmatrix}\operatorname{diag}(\mathcal{P}_r, \mathcal{Q}_r), \tag{24b}$$

in which

$$\Phi = \begin{bmatrix}\mathcal{E}_{(\mathrm{e})} & 0\\ 0 & \mathcal{E}_{(\mathrm{f})}\end{bmatrix} - \begin{bmatrix}0 & \mathcal{X}_{(\mathrm{e})}\\ \mathcal{X}_{(\mathrm{f})} & 0\end{bmatrix}\begin{bmatrix}\mathcal{M}_{(\mathrm{f})}^{-1} & 0\\ 0 & \mathcal{M}_{(\mathrm{e})}^{-1}\end{bmatrix}\begin{bmatrix}0 & \mathcal{Z}_{(\mathrm{f})}\\ \mathcal{Z}_{(\mathrm{e})} & 0\end{bmatrix}$$
$$= \begin{bmatrix}\mathcal{E}_{(\mathrm{e})} - \mathcal{X}_{(\mathrm{e})}\mathcal{M}_{(\mathrm{e})}^{-1}\mathcal{Z}_{(\mathrm{e})} & 0\\ 0 & \mathcal{E}_{(\mathrm{f})} - \mathcal{X}_{(\mathrm{f})}\mathcal{M}_{(\mathrm{f})}^{-1}\mathcal{Z}_{(\mathrm{f})}\end{bmatrix}$$
$$\equiv \operatorname{diag}(\Phi_{(\mathrm{e})}, \Phi_{(\mathrm{f})}). \tag{24c}$$

As a result, the electric and magnetic fields can be restored efficiently by

$$\begin{bmatrix}\mathbf{e}_e^\top & \mathbf{e}_f^\top & \mathbf{h}_f^\top & \mathbf{h}_e^\top\end{bmatrix}^\top = \imath\begin{bmatrix}-\mathcal{Z} & -I_{24n}\\ \mathcal{E} & \mathcal{X}\end{bmatrix}^{-1}\operatorname{diag}(\mathcal{P}_r, \mathcal{Q}_r)\,\mathbf{y}_r.$$

Moreover, combined with the derivations in Appendix D, the NFGEP (24a) can be rewritten as

$$\begin{bmatrix}A_{(\mathrm{f})} & 0\\ 0 & A_{(\mathrm{e})}\end{bmatrix}\tilde{\mathbf{y}}_r = \omega\left(\imath\begin{bmatrix}0 & B\\ B & 0\end{bmatrix}\right)\tilde{\mathbf{y}}_r, \quad \mathbf{y}_r = \Pi_2^\top\tilde{\mathbf{y}}_r, \tag{25a}$$

where $\Pi_2 = [\mathbf{e}_1, \mathbf{e}_3, \mathbf{e}_4, \mathbf{e}_2]_{4\times 4} \otimes I_{8n} \in \mathbb{R}^{32n\times 32n}$,

$$A_{(\mathrm{f})} = \operatorname{diag}(P_r^*, P_r^*)\begin{bmatrix}\mathcal{F}_{(\mathrm{f})} & \mathcal{M}_{(\mathrm{f})}^{-1}\mathcal{Z}_{(\mathrm{f})}\Phi_{(\mathrm{f})}^{-1}\\ \Phi_{(\mathrm{f})}^{-1}\mathcal{X}_{(\mathrm{f})}\mathcal{M}_{(\mathrm{f})}^{-1} & \Phi_{(\mathrm{f})}^{-1}\end{bmatrix}\operatorname{diag}(P_r, P_r), \tag{25b}$$

$$A_{(\mathrm{e})} = \operatorname{diag}(Q_r^*, Q_r^*)\begin{bmatrix}\mathcal{F}_{(\mathrm{e})} & \mathcal{M}_{(\mathrm{e})}^{-1}\mathcal{Z}_{(\mathrm{e})}\Phi_{(\mathrm{e})}^{-1}\\ \Phi_{(\mathrm{e})}^{-1}\mathcal{X}_{(\mathrm{e})}\mathcal{M}_{(\mathrm{e})}^{-1} & \Phi_{(\mathrm{e})}^{-1}\end{bmatrix}\operatorname{diag}(Q_r, Q_r), \tag{25c}$$

$$\mathcal{F}_{(\mathrm{c})} = \mathcal{M}_{(\mathrm{c})}^{-1} + \mathcal{M}_{(\mathrm{c})}^{-1}\mathcal{Z}_{(\mathrm{c})}\Phi_{(\mathrm{c})}^{-1}\mathcal{X}_{(\mathrm{c})}\mathcal{M}_{(\mathrm{c})}^{-1}, \quad \mathrm{c} = \mathrm{e}\ \text{or}\ \mathrm{f}, \tag{25d}$$

$$B = \begin{bmatrix}0 & \Sigma_r^{-1}\\ -\Sigma_r^{-1} & 0\end{bmatrix}. \tag{25e}$$

The nonzero eigenvalues of the MEP (4) are the same as those of the NFGEP (25) and form pairs and quadruplets, as in Theorem 2.

Theorem 6. *Assume $\xi(\mathbf{r}) = \zeta(\mathbf{r})^*$. Then the NFGEP (25) has eigenvalues $\{\omega, -\omega\}$ if $\omega \in \mathbb{R} \cup \imath\mathbb{R}$ and $\{\omega, -\omega, \bar{\omega}, -\bar{\omega}\}$ if $\omega \in \mathbb{C}\backslash(\mathbb{R} \cup \imath\mathbb{R})$.*

Proof. See Appendix C.3. □

To conclude, the matrix $\mathcal{C}$ in this section is singular and one-third of its eigenvalues are zero; thus, a null-space free technique is a suitable method to accelerate the procedure of convergence of eigenvalues of the smallest modulus. If $\mathcal{E}_{(\mathrm{e})}$, $\mathcal{E}_{(\mathrm{f})}$, $\mathcal{M}_{(\mathrm{e})}$, $\mathcal{M}_{(\mathrm{f})}$, $\Phi_{(\mathrm{e})}$, $\Phi_{(\mathrm{f})}$ in (24c) are HPD, $\mathcal{Z}_{(\mathrm{e})}^* = \mathcal{X}_{(\mathrm{e})}$, and $\mathcal{Z}_{(\mathrm{f})}^* = \mathcal{X}_{(\mathrm{f})}$, then from (D.1), $A_{(\mathrm{f})}$ and $A_{(\mathrm{e})}$ in (25b) and (25c), respectively, are also HPD. This implies that all eigenvalues of the NFGEP (25) are real.

The iterative eigensolver can now be applied to solve (25). In the iterative processes, the matrix–vector multiplications $T\mathbf{q}$ and $T^*\mathbf{p}$ for given vectors $\mathbf{p}$ and $\mathbf{q}$ can be performed by a sequence of elementwise multiplications, diagonal matrix–vector multiplications and one-dimensional backward and forward FFTs, the details of which can be found in Algorithm 3 and 4 in [22], respectively.

5. Numerical results

In this section, with the aid of the bi-Lebedev scheme, we present some numerical results of the MEP (4) with 3D reciprocal bi-anisotropic chiral media using FD methods.

We take the media shown in Fig. 2(a) with the FCC lattice as an example. Recall that the cubic working cell in Fig. 2(a) is constructed from the primitive cell, usually a slanted parallelepiped, of any Bravais lattice by some cutting and pasting [21]. The working cell naturally defines a Cartesian coordinate system in which the lattice translation vectors of the FCC lattice are $a_1 = a[\frac{1}{\sqrt{2}}, -\frac{1}{\sqrt{6}}, \frac{1}{\sqrt{3}}]^\top$, $a_2 = a[\frac{1}{\sqrt{2}}, \frac{1}{\sqrt{6}}, -\frac{1}{\sqrt{3}}]^\top$, $a_3 = a[0, \sqrt{\frac{2}{3}}, \frac{1}{\sqrt{3}}]^\top$. Here, a is the lattice constant and is set to 1. The reciprocal bi-anisotropic chiral medium occupies the shadow region in the working cell in Fig. 2(a), consisting of a dielectric sphere and a cylinder with radii $r_s = 0.11a$ and $r_c = 0.08a$, respectively, while the background medium is air.

The magnetoelectric coupling $\xi(\boldsymbol{r})$ and $\zeta(\boldsymbol{r})$ are defined in (3), and the permeability is simply $\mu = I_3$. We use $\tilde{\varepsilon} = 2.5 \oplus \begin{bmatrix}2.5 & 2+0.5\imath\\ 2-0.5\imath & 5.5\end{bmatrix}$ to generate the desired permittivity tensor.

Unless otherwise specified, the results in this section are obtained given the Bloch wave vector $\boldsymbol{k} = \frac{13}{14}Q[0, 1, 0]^\top + \frac{1}{14}Q[\frac{1}{4}, 1, \frac{1}{4}]^\top$ with $Q = \sqrt{2}\begin{bmatrix}\frac{1}{2} & \frac{1}{2} & 0\\ -\frac{1}{2\sqrt{3}} & \frac{1}{2\sqrt{3}} & \frac{1}{\sqrt{3}}\\ \frac{1}{\sqrt{6}} & -\frac{1}{\sqrt{6}} & \frac{1}{\sqrt{6}}\end{bmatrix}$. Furthermore,

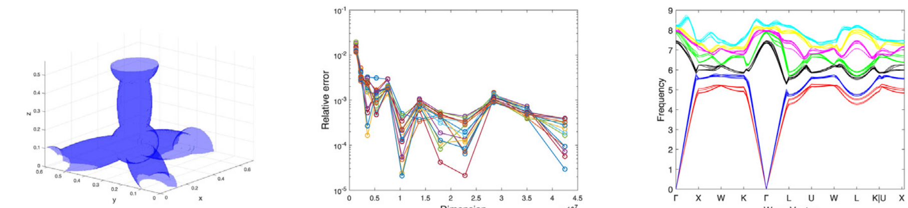

(a) Working cell of the FCC lattice (b) Relative error vs. various dimensions (c) Band structure

Fig. 2. (a) Working cell of the FCC lattice [2]; (b) Relative errors of eigenvalues λ_i, $i = 1, \ldots, 16$, with matrix dimension $48 \times (6m)^3$ for $m = 5, 6, \ldots, 16$; (c) Band structure of the reciprocal bi-anisotropic chiral media with $\gamma = 1.0$.

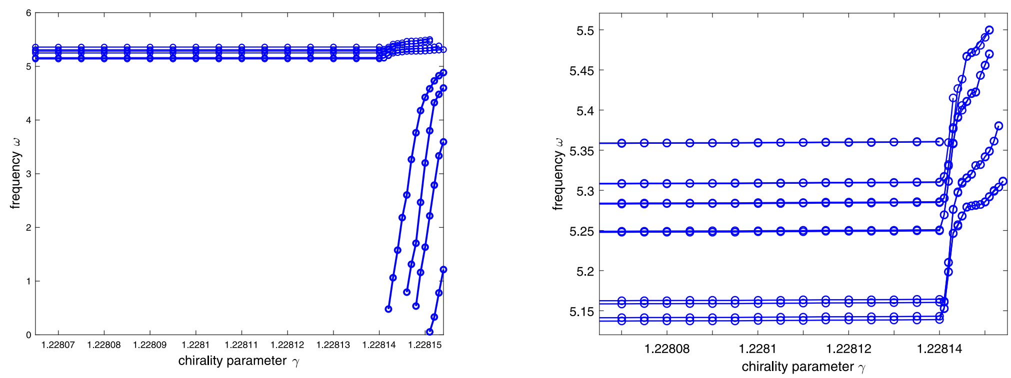

(a) The bifurcation diagram of smallest few positive eigenvalues. (b) Zooming-in on the upper part of the bifurcation diagram.

Fig. 3. (a) Demonstration of newborn positive eigenvalues when $\gamma \geq 1.228142$; (b) Some original eigenvalues are pushed towards $+\infty$.

we take $n_1 = n_2 = n_3 = 60$; accordingly, the matrix dimensions of the GEP in (15) and the NFGEP in (24) are 10,368,000 and 6,912,000, respectively. The inexact SIRA [23,24] in conjunction with the MINRES solver [25] and FFT-based matrix–vector multiplication [22] are utilized to solve the NFGEP in (25). The stopping tolerances of the inexact SIRA and the MINRES are set to 10^{-11} and 10^{-3}, respectively.

All numerical results are obtained on a computer with an Intel Xeon E5-2650 v4 2.20 GHz 24-core CPU, 512 GB DDR4 memory, Ubuntu 16.04.4 LTS OS, and an NVIDIA Tesla P100 GPU.

5.1. Results for the bi-anisotropic model with the HPD weight matrix

First, we validate the convergence of the eigenvalues obtained via the bi-Lebedev scheme when the weight matrix is HPD in which case (25) has only real eigenvalues. Specifically, we set $\gamma = 1.0$, a small random number, and $\varepsilon = Q\tilde{\varepsilon}Q^\top$, and we compute the 16 smallest positive eigenvalues for (25) for $n_1 = n_2 = n_3 = 6m$ with $m = 5, 6, \ldots, 16$. The relative errors defined by $|\lambda_{m+1} - \lambda_m|/|\lambda_m|$ are shown in Fig. 2(b), which clearly demonstrates the nice convergence property of the eigenvalues.

Second, we compute the band structure of the 3D reciprocal bi-anisotropic chiral media with $\gamma = 1.0$ and $\varepsilon = Q\tilde{\varepsilon}Q^\top$. Now that $\Phi_{(e)}$ and $\Phi_{(f)}$ in (24c) are HPD, we can relatively easily compute the smallest 56 positive eigenvalues of (25). On the basis of the band structure plotted in Fig. 2(c), it appears that the bi-anisotropic complex media with the specific parameters does NOT possess a bandgap.

5.2. Bifurcation of eigenvalues

The smallest eigenvalue of $\tilde{\varepsilon}$ is approximately 1.4505; thus, the weight matrix $\begin{bmatrix} Q\tilde{\varepsilon}Q^\top & \imath\gamma I_3 \\ -\imath\gamma I_3 & I_3 \end{bmatrix}$ becomes singular if $\gamma = \gamma_* \approx \sqrt{1.4505} \approx 1.20436$. According to Theorems 3.2 and 3.3 in [2], at this moment, the pencil $\mathcal{A}_r(\gamma_*) - \omega\imath\mathcal{B}_r(\gamma_*)$ in (25) has a large number of 2×2 Jordan blocks at $\omega = \infty$, which are, however, inaccessible in numerical calculations.

The following situation is more relevant to our calculations. When $\gamma = \gamma_* + 0^+$, the Jordan blocks suddenly generate an abundance of eigenvalue tetrads $\{\omega, -\omega, \bar{\omega}, -\bar{\omega}\}$ that are all crowded around $\imath\infty$ and have very small real parts. As γ gradually extends beyond γ_*, some of the tetrads $\{\omega, -\omega, \bar{\omega}, -\bar{\omega}\}$ collide near the origin and then move along the real axis in the positive and negative directions, respectively, which can be numerically accessible.

In practice, it remains challenging to find the exact γ for the bifurcation described above to occur for the first time. After extensive manual intervention, we identify the interval, *i.e.*, $[1.2307, 1.2309]$ for this specific case, in which such γ lies. Then, we calculate the smallest few positive eigenvalues for dense and uniform samplings of γ in $[1.2307, 1.2309]$ and plot the results in Fig. 3(a). Finally, we find that when $\gamma \approx 1.228142$, a new positive eigenvalue is born for the first time, with a considerably lower frequency than the original ground state, as shown in Fig. 3(a). In addition, from Fig. 3(b), it appears as if the newborn positive eigenvalues have pushed some of the original ones slightly toward $+\infty$. Conversely, these original eigenfields are rather stable in the sense that they are resistant to the perturbation of γ and the ensuing change in the nature of the GEP, in striking contrast to the dramatic change in the eigenfrequency of the newborn ground state with respect to a tiny perturbation of γ.

5.3. Localization property of newborn eigenfields

First, we use a volumetric slice plot to qualitatively explore the localization property of eigenfields $\mathbf{x}_1$, $\mathbf{x}_2$, $\mathbf{x}_3$ and $\mathbf{x}_4$ associated the smallest positive eigenvalues $\lambda_1 = 5.12924$, $\lambda_1 = 4.8385$, $\lambda_1 = 0.8627$, and $\lambda_1 = 0.4787$ of four GEPs with (a) $\varepsilon = \tilde{\varepsilon}$,

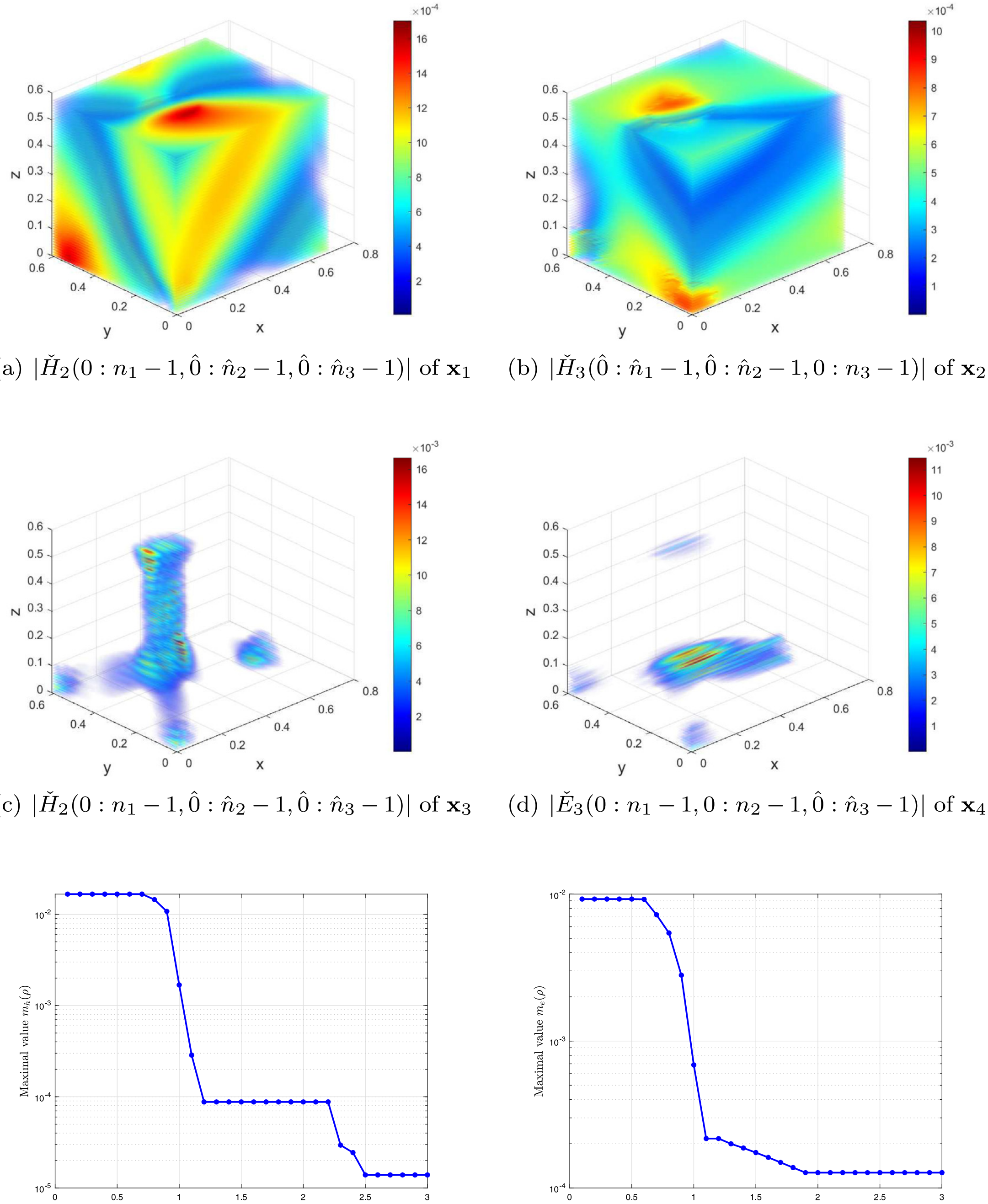

(a) $|\check{H}_2(0:n_1-1,\hat{0}:\hat{n}_2-1,\hat{0}:\hat{n}_3-1)|$ of $\mathbf{x}_1$ (b) $|\check{H}_3(\hat{0}:\hat{n}_1-1,\hat{0}:\hat{n}_2-1,0:n_3-1)|$ of $\mathbf{x}_2$

(c) $|\check{H}_2(0:n_1-1,\hat{0}:\hat{n}_2-1,\hat{0}:\hat{n}_3-1)|$ of $\mathbf{x}_3$ (d) $|\check{E}_3(0:n_1-1,0:n_2-1,\hat{0}:\hat{n}_3-1)|$ of $\mathbf{x}_4$

(e) $m_h(\rho)$ vs. ρ of $\mathbf{x}_3$ (f) $m_e(\rho)$ vs. ρ of $\mathbf{x}_4$

Fig. 4. The magnitude of selective components of the eigenvectors $\mathbf{x}_i$, $i = 1, \ldots, 4$, $m_h(\rho)$ for $\mathbf{x}_3$ and $m_e(\rho)$ for $\mathbf{x}_4$ outside $V(\rho)$.

$\gamma = 0.275$, (b) $\varepsilon = Q\tilde{\varepsilon}Q^\top$, $\gamma = 1.0$, (c) $\varepsilon = \tilde{\varepsilon}$, $\gamma = 1.23399$ and (d) $\varepsilon = Q\tilde{\varepsilon}Q^\top$, $\gamma = 1.228142$, respectively. Note that $\mathbf{x}_3$ and $\mathbf{x}_4$ are newborn ground states.

In Fig. 4(a), according to (6), we plot the magnitude of the H_2 component of $\mathbf{x}_1$ at grid points belonging to subgrid 1. In Fig. 4(b), we plot the magnitude of the H_3 component of $\mathbf{x}_2$ at the face centers. Clearly, these eigenfields are distributed throughout Ω_c as shown in Fig. 2(a).

The magnitude of the H_2 component of $\mathbf{x}_3$ at grid points belonging to subgrid 1 and the magnitude of the E_3 component of $\mathbf{x}_4$ at the midpoints of edges can be found in Figs. 4(c) and 4(d), respectively. These two figures indicate that the eigenfields $\mathbf{x}_3$ and $\mathbf{x}_4$ could be entirely within the bi-anisotropic medium compared with the shadow region in Fig. 2(a).

To quantitatively measure the localization of $\mathbf{x}_3$ and $\mathbf{x}_4$, we introduce a scaling parameter $\rho > 0$ and denote by $V(\rho)$ the region occupied by spheres and cylinders with radius $r_s = \rho \times 0.11a$ and $r_c = \rho \times 0.08a$, respectively. Note that $V(\rho)$ with $\rho > 1$ contains the original region, $V(1)$, and its neighborhood. Let

$$m_e(\rho) = \max_{i=0,\ldots,n_1-1, j=0,\ldots,n_2-1, k=0,\ldots,n_3-1} \{|\check{E}_3(i,j,\hat{k})| \,|\, (i,j,\hat{k}) \in \Omega_c \backslash V(\rho)|\},$$

$$m_h(\rho) = \max_{i=0,\ldots,n_1-1, j=0,\ldots,n_2-1, k=0,\ldots,n_3-1} \{|\check{H}_2(i,\hat{j},\hat{k})| \,|\, (i,\hat{j},\hat{k}) \in \Omega_c \backslash V(\rho)|\}.$$

We plot $m_h(\rho)$ for $\mathbf{x}_3$ and $m_e(\rho)$ for $\mathbf{x}_4$ versus ρ in Figs. 4(e) and 4(f), respectively. Clearly, $m_h(\rho)$ and $m_e(\rho)$ drop substantially

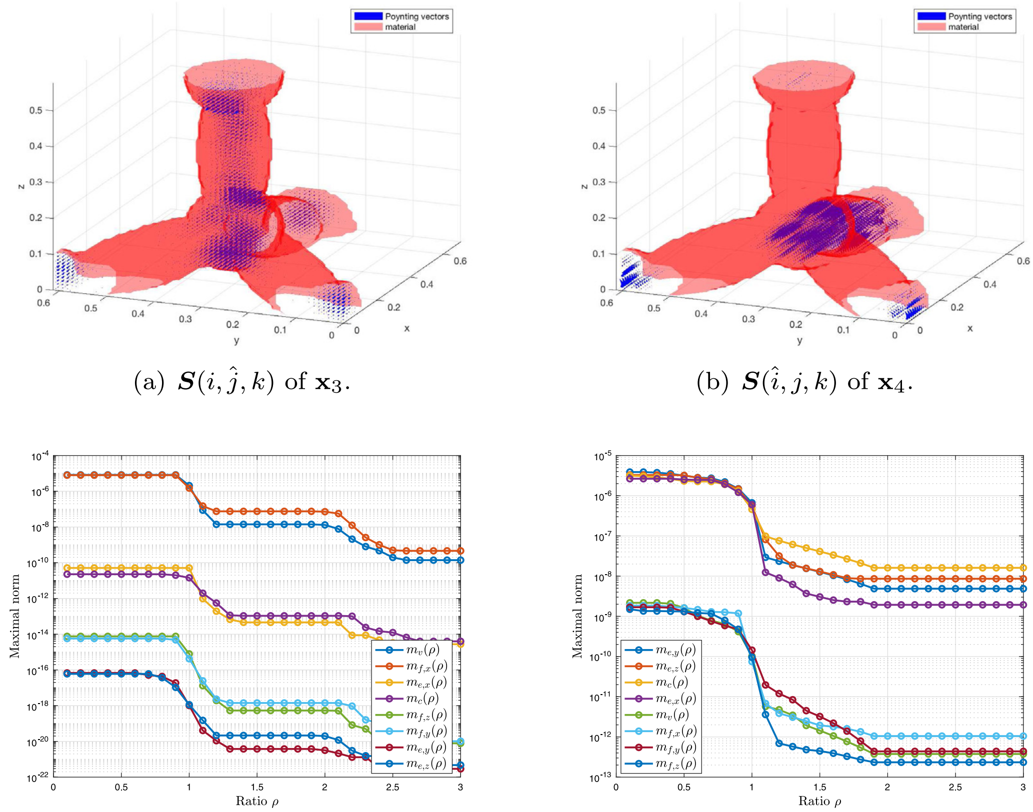

(a) $\boldsymbol{S}(i,\hat{j},k)$ of $\mathbf{x}_3$. (b) $\boldsymbol{S}(\hat{i},j,k)$ of $\mathbf{x}_4$.

(c) Maximal norms of $\boldsymbol{S}$ of $\mathbf{x}_3$ vs. ρ (d) Maximal norms of $\boldsymbol{S}$ of $\mathbf{x}_4$ vs. ρ

Fig. 5. $\boldsymbol{S}$ of $\mathbf{x}_3$ and $\mathbf{x}_4$ and the maximal norm of $\boldsymbol{S}$ outside $V(\rho)$.

around $\rho = 1.2$, which means that E_3 and H_2 are localized in the chiral medium.

In fact, in addition to $\check{H}_2(0 : n_1 - 1, \hat{0} : \hat{n}_2 - 1, \hat{0} : \hat{n}_3 - 1)$ and $\check{E}_3(0 : n_1 - 1, 0 : n_2 - 1, \hat{0} : \hat{n}_3 - 1)$, other portions of $\mathbf{x}_3$ and $\mathbf{x}_4$ are similarly localized in the chiral medium and its neighborhood.

5.4. Poynting vectors

For a plane-wave electromagnetic field, the Poynting vector $\boldsymbol{S} = \frac{1}{2}\Re(\boldsymbol{E} \times \bar{\boldsymbol{H}})$ represents the flow of energy carried by the electromagnetic field along the wave vector direction, and its magnitude equals the intensity of the field. However, for an electromagnetic field subject to the quasiperiodic condition (5), this characteristic is generally invalid.

Now that we have the full components of the collocated $\boldsymbol{E}$-field and $\boldsymbol{H}$-field belonging to the same eigenfield, the Poynting vector $\boldsymbol{S}$ can be calculated with little additional effort. Here, we report the numerical behavior of the Poynting vector of the eigenvectors $\mathbf{x}_3$ and $\mathbf{x}_4$ in Section 5.3.

To quantitatively measure the localization of $\mathbf{x}_3$ and $\mathbf{x}_4$, as seen in Figs. 5(a) and 5(b), we define

$$m_{e,x}(\rho) = \max_{i=0,\ldots,n_1-1,j=0,\ldots,n_2-1,k=0,\ldots,n_3-1} \{\|\boldsymbol{S}(\hat{i},j,k)\|_2 | (\hat{i},j,k) \in \Omega_c \backslash V(\rho)\},$$

where $\|\cdot\|_2$ is the Euclidean norm. Similarly, let $m_{e,y}(\rho)$, $m_{e,z}(\rho)$, $m_c(\rho)$, $m_{f,x}(\rho)$, $m_{f,y}(\rho)$, $m_{f,z}(\rho)$ and $m_v(\rho)$ denote the maximal norm of $\boldsymbol{S}$ at points $(i,\hat{j},k)$, $(i,j,\hat{k})$, $(\hat{i},\hat{j},\hat{k})$, $(i,\hat{j},\hat{k})$, $(\hat{i},j,\hat{k})$, $(\hat{i},\hat{j},k)$, and $(i,j,k) \in \Omega_c \backslash V(\rho)$, $i = 0,\ldots,n_1-1$, $j = 0,\ldots,n_2-1$, $k = 0,\ldots,n_3-1$, respectively. From the curves of these maximal norms versus ρ in Figs. 5(c) and 5(d), we can clearly see, similar to the eigenfield itself, the associated Poynting vector is also concentrated in the chiral medium. Furthermore, we can reveal more details of these Poynting vectors. From Figs. 5(c) and 5(d), we see that the maximal norms of $\boldsymbol{S}(\hat{i},j,k)$ and $\boldsymbol{S}(i,j,k)$ for $\mathbf{x}_3$, and $\boldsymbol{S}(\hat{i},j,k)$, $\boldsymbol{S}(i,\hat{j},k)$, $\boldsymbol{S}(i,j,\hat{k})$ and $\boldsymbol{S}(\hat{i},\hat{j},\hat{k})$ for $\mathbf{x}_4$, $i = 0,\ldots,n_1-1$, $j = 0,\ldots,n_2-1$, $k = 0,\ldots,n_3-1$, are $\mathcal{O}(10^{-6})$. Hence, we zoom in on only the region of high density to display $\boldsymbol{S}(\hat{i},j,k)$ and $\boldsymbol{S}(i,j,k)$ for $\mathbf{x}_3$, and, $\boldsymbol{S}(\hat{i},j,k)$, $\boldsymbol{S}(i,\hat{j},k)$, $\boldsymbol{S}(i,j,\hat{k})$ and $\boldsymbol{S}(\hat{i},\hat{j},\hat{k})$ for $\mathbf{x}_4$ in Figs. 6(a) and 6(b), respectively. The results show that all arrows have exciting patterns. As shown in the left two subfigures of Fig. 6(c) for $\mathbf{x}_3$, the Poynting vectors form symmetric patterns on the xy-plane for a fixed z-axis. The modes on the top and bottom have opposite directions. The right subfigure shows that the modes from top to bottom form an s-shape pattern. The Poynting vector of the eigenvector $\mathbf{x}_4$ shown in Fig. 6(b) has more diverse shapes. We zoom in on four representative shapes and display them in Fig. 6(d). The results demonstrate that each pattern is generated by a different rotation. We find that some of the patterns in Fig. 6(b) have a similar rotation style, while some of them are different.

6. Conclusion

In this paper, we have established the FD discretization of (4) by virtue of the bi-Lebedev scheme and proposed a null-space free method to compute the band structure of 3D periodic bi-anisotropic complex media. Although we take only the case with a scalar magnetoelectric coupling constant and FCC lattice as an example, it is not difficult to see that the formulas and algorithms

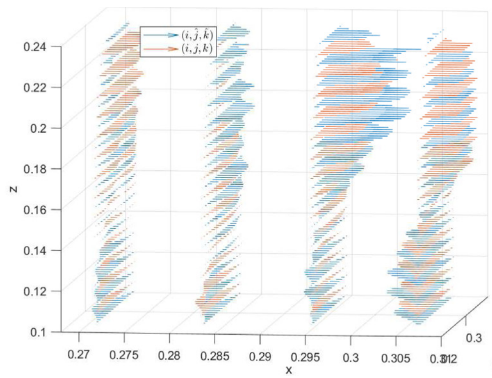

(a) Poynting vectors of $\boldsymbol{S}$ at $(i, \hat{j}, \hat{k})$ and (i, j, k) for $\mathbf{x}_3$.

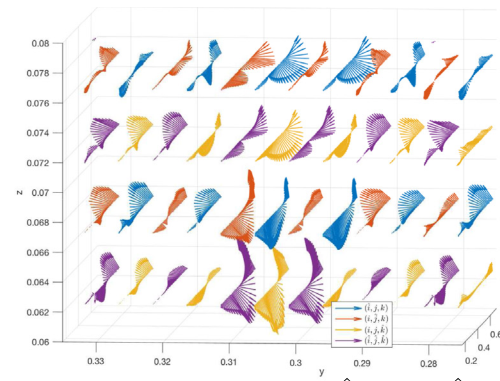

(b) Poynting vectors of $\boldsymbol{S}$ at $(\hat{\imath}, j, k)$, $(i, \hat{j}, k)$, $(i, j, \hat{k})$, $(\hat{\imath}, \hat{j}, \hat{k})$ for $\mathbf{x}_4$.

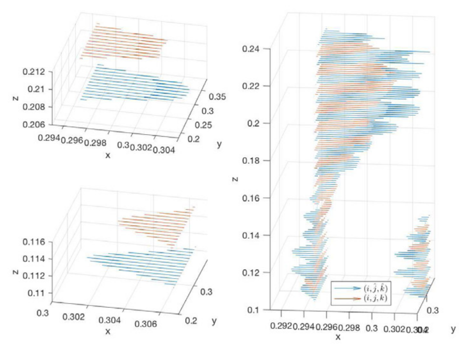

(c) Zooming-in on (a)

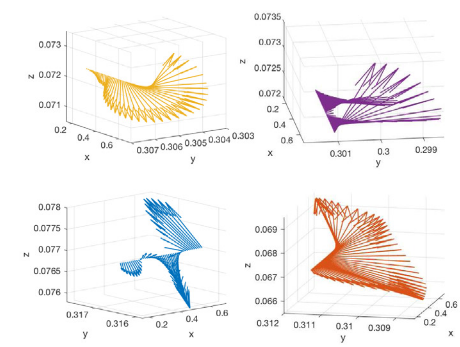

(d) Zooming-in on (b)

Fig. 6. Details of Poynting vector S of $\mathbf{x}_3$ and $\mathbf{x}_4$ in the localized region.

involved can be readily adapted for 3D bi-anisotropic complex media with very general magnetoelectric coupling tensors and other Bravais lattices. Here, a formulation of the discrete single-curl operator can easily be built from the counterpart in the standard Yee scheme. Moreover, many apparatuses, notably, the SVD of the discrete single-curl operator and NFGEP, developed for Yee's scheme [1] can readily be generalized to the bi-Lebedev scheme, as shown in Section 4. The combination of all these building blocks results in a clean and fast method for the band structure calculation of 3D bi-anisotropic complex media.

With sound mathematical theory as guidance, we have predicted and numerically verified the existence of some exotic eigenfields that are highly concentrated in the 3D reciprocal bi-isotropic chiral material in [2]. Since there are many more parameters in the permittivity tensor ε, permeability tensor μ and magnetoelectric coupling tensors ξ and ζ selected in the 3D bi-anisotropic model, the approach used to make the weight matrix $\begin{bmatrix} \varepsilon & \xi \\ \zeta & \mu \end{bmatrix}$ indefinite is more flexible and the resulting models are supposedly more realizable. In this work, we have taken a solid step forward in this direction. That is, we have found a smaller critical chirality parameter $\gamma_* \approx 1.20436$, even though the largest entry of ε is 5.5, and have captured possibly the first newborn ground state at $\gamma = 1.228142$. Moreover, the spatial distribution of the Poynting vector corresponding to the exotic eigenfield displays some intriguing patterns. We plan to study these patterns, especially their physical roots and implications, in the future. Last, we expect that the physical phenomena observed in this work will motivate further theoretical and experimental investigations. It would be exciting to see its application in the field of metamaterial physics and engineering.

Declaration of competing interest

The authors declare that they have no known competing financial interests or personal relationships that could have appeared to influence the work reported in this paper.

Acknowledgments

T. Li was supported in part by the National Natural Science Foundation of China (NSFC) 11971105. T.-M. Huang was partially supported by the Ministry of Science and Technology (MoST), Taiwan 108-2115-M-003-012-MY2. W.-W. Lin was partially supported by MoST, Taiwan 106-2628-M-009-004-. H. Tian was supported by MoST, Taiwan 107-2811-M-009-002-. This work was also partially supported by the National Centre of Theoretical Sciences (NCTS) in Taiwan, ST Yau Centre in Taiwan, and the Shing-Tung Yau Center and the Big Data Computing Center of Southeast University. The numerical calculation of this work was partially performed on TianHe-2, thanks to the support of the National Supercomputing Center in Guangzhou (NSCC-GZ), People's Republic of China.

Appendix A. Definition of matrix $\mathcal{S}^{(\mathbf{c})}(s)$ for c = e or f

Define

$$S_{pq}^{(\mathbf{e})}(x, s) = \operatorname{diag}\left(\check{s}_{pq}(\hat{0} : \hat{n}_1 - 1, 0 : n_2 - 1, 0 : n_3 - 1)\right), \tag{A.1a}$$

$$S_{pq}^{(\mathrm{e})}(y,s) = \mathrm{diag}\left(\check{s}_{pq}(0:n_1-1,\hat{0}:\hat{n}_2-1,0:n_3-1)\right), \quad \text{(A.1b)}$$

$$S_{pq}^{(\mathrm{e})}(z,s) = \mathrm{diag}\left(\check{s}_{pq}(0:n_1-1,0:n_2-1,\hat{0}:\hat{n}_3-1)\right), \quad \text{(A.1c)}$$

$$S_{pq}^{(\mathrm{e})}(s) = \mathrm{diag}\left(\check{s}_{pq}(\hat{0}:\hat{n}_1-1,\hat{0}:\hat{n}_2-1,\hat{0}:\hat{n}_3-1)\right), \quad \text{(A.1d)}$$

$$S_{pq}^{(\mathrm{f})}(x,s) = \mathrm{diag}\left(\check{s}_{pq}(0:n_1-1,\hat{0}:\hat{n}_2-1,\hat{0}:\hat{n}_3-1)\right), \quad \text{(A.1e)}$$

$$S_{pq}^{(\mathrm{f})}(y,s) = \mathrm{diag}\left(\check{s}_{pq}(\hat{0}:\hat{n}_1-1,0:n_2-1,\hat{0}:\hat{n}_3-1)\right), \quad \text{(A.1f)}$$

$$S_{pq}^{(\mathrm{f})}(z,s) = \mathrm{diag}\left(\check{s}_{pq}(\hat{0}:\hat{n}_1-1,\hat{0}:\hat{n}_2-1,0:n_3-1)\right), \quad \text{(A.1g)}$$

$$S_{pq}^{(\mathrm{f})}(s) = \mathrm{diag}\left(\check{s}_{pq}(0:n_1-1,0:n_2-1,0:n_3-1)\right), \quad \text{(A.1h)}$$

for $p,\ q = 1,2,3$ and

$$\mathcal{S}^{(\mathrm{C})}(s) = \left[\mathcal{S}_{uv}^{(\mathrm{C})}(s)\right]_{u,v=1}^{4} \in \mathbb{C}^{12n\times 12n},$$

for $\mathrm{c} = \mathrm{e}$ or f with

$$\mathcal{S}_{11}^{(\mathrm{C})}(s) = \mathrm{diag}\left(S_{11}^{(\mathrm{C})}(x,s), S_{22}^{(\mathrm{C})}(y,s), S_{33}^{(\mathrm{C})}(z,s)\right),$$

$$\mathcal{S}_{22}^{(\mathrm{C})}(s) = \mathrm{diag}\left(S_{11}^{(\mathrm{C})}(y,s), S_{22}^{(\mathrm{C})}(x,s), S_{33}^{(\mathrm{C})}(s)\right),$$

$$\mathcal{S}_{33}^{(\mathrm{C})}(s) = \mathrm{diag}\left(S_{11}^{(\mathrm{C})}(z,s), S_{22}^{(\mathrm{C})}(s), S_{33}^{(\mathrm{C})}(x,s)\right),$$

$$\mathcal{S}_{44}^{(\mathrm{C})}(s) = \mathrm{diag}\left(S_{11}^{(\mathrm{C})}(s), S_{22}^{(\mathrm{C})}(z,s), S_{33}^{(\mathrm{C})}(y,s)\right),$$

and

$$\mathcal{S}_{12}^{(\mathrm{C})}(s) = \begin{bmatrix} 0 & S_{12}^{(\mathrm{C})}(x,s) & 0 \\ S_{21}^{(\mathrm{C})}(y,s) & 0 & 0 \\ 0 & 0 & 0 \end{bmatrix} = \mathcal{S}_{21}^{(\mathrm{C})}(s)^*,$$

$$\mathcal{S}_{13}^{(\mathrm{C})}(s) = \begin{bmatrix} 0 & 0 & S_{13}^{(\mathrm{C})}(x,s) \\ 0 & 0 & 0 \\ S_{31}^{(\mathrm{C})}(z,s) & 0 & 0 \end{bmatrix} = \mathcal{S}_{31}^{(\mathrm{C})}(s)^*,$$

$$\mathcal{S}_{14}^{(\mathrm{C})}(s) = \begin{bmatrix} 0 & 0 & 0 \\ 0 & 0 & S_{23}^{(\mathrm{C})}(y,s) \\ 0 & S_{32}^{(\mathrm{C})}(z,s) & 0 \end{bmatrix} = \mathcal{S}_{41}^{(\mathrm{C})}(s)^*,$$

$$\mathcal{S}_{23}^{(\mathrm{C})}(s) = \begin{bmatrix} 0 & 0 & 0 \\ 0 & 0 & S_{23}^{(\mathrm{C})}(x,s) \\ 0 & S_{32}^{(\mathrm{C})}(s) & 0 \end{bmatrix} = \mathcal{S}_{32}^{(\mathrm{C})}(s)^*,$$

$$\mathcal{S}_{24}^{(\mathrm{C})}(s) = \begin{bmatrix} 0 & 0 & S_{13}^{(\mathrm{C})}(y,s) \\ 0 & 0 & 0 \\ S_{31}^{(\mathrm{C})}(s) & 0 & 0 \end{bmatrix} = \mathcal{S}_{42}^{(\mathrm{C})}(s)^*,$$

$$\mathcal{S}_{34}^{(\mathrm{C})}(s) = \begin{bmatrix} 0 & S_{12}^{(\mathrm{C})}(z,s) & 0 \\ S_{21}^{(\mathrm{C})}(s) & 0 & 0 \\ 0 & 0 & 0 \end{bmatrix} = \mathcal{S}_{43}^{(\mathrm{C})}(s)^*.$$

With

$$\mathcal{E}_{u,v}^{(\mathrm{C})} = \mathcal{S}_{u,v}^{(\mathrm{C})}(\varepsilon),\ \mathcal{M}_{u,v}^{(\mathrm{C})} = \mathcal{S}_{u,v}^{(\mathrm{C})}(\mu),\ \mathcal{X}_{u,v}^{(\mathrm{C})} = \mathcal{S}_{u,v}^{(\mathrm{C})}(\xi),\ \mathcal{Z}_{u,v}^{(\mathrm{C})} = \mathcal{S}_{u,v}^{(\mathrm{C})}(\zeta),$$

for $\mathrm{c} = \mathrm{e}$ or f, $u, v = 1,\ldots,4$, we define

$$\mathcal{E}_{(\mathrm{C})} = [\mathcal{E}_{u,v}^{(\mathrm{C})}]_{u,v=1}^{4},\ \mathcal{M}_{(\mathrm{C})} = [\mathcal{M}_{u,v}^{(\mathrm{C})}]_{u,v=1}^{4},\ \mathcal{X}_{(\mathrm{C})} = [\mathcal{X}_{u,v}^{(\mathrm{C})}]_{u,v=1}^{4},$$
$$\mathcal{Z}_{(\mathrm{C})} = [\mathcal{Z}_{u,v}^{(\mathrm{C})}]_{u,v=1}^{4}.$$

Appendix B. Discretization of MEP with 3D Bi-anisotropic complex media

B.1. Matrix representation of $\nabla\times\boldsymbol{E} = \imath\omega\boldsymbol{B}$ at face centers

• Subgrid 1 (Fig. 1(b)):

Consider the FD discretization of (1a) by the standard Yee scheme at face centers $(i,\hat{j},\hat{k})$, $(\hat{i},j,\hat{k})$ and $(\hat{i},\hat{j},k)$, respectively.

$$\frac{E_3(i,j+1,\hat{k}) - E_3(i,j,\hat{k})}{\delta_y} - \frac{E_2(i,\hat{j},k+1) - E_2(i,\hat{j},k)}{\delta_z}$$
$$= \imath\omega B_1(i,\hat{j},\hat{k}), \quad \text{(B.1a)}$$

$$\frac{E_1(\hat{i},j,k+1) - E_1(\hat{i},j,k)}{\delta_z} - \frac{E_3(i+1,j,\hat{k}) - E_3(i,j,\hat{k})}{\delta_x}$$
$$= \imath\omega B_2(\hat{i},j,\hat{k}), \quad \text{(B.1b)}$$

$$\frac{E_2(i+1,\hat{j},k) - E_2(i,\hat{j},k)}{\delta_x} - \frac{E_1(\hat{i},j+1,k) - E_1(\hat{i},j,k)}{\delta_y}$$
$$= \imath\omega B_3(\hat{i},\hat{j},k), \quad \text{(B.1c)}$$

for $i = 0,\ldots,n_1-1$, $j = 0,\ldots,n_2-1$ and $k = 0,\ldots,n_3-1$. From (2) and (3), it holds that

$$B_1(i,\hat{j},\hat{k}) = (\zeta_{11}E_1 + \zeta_{12}E_2 + \zeta_{13}E_3 + \mu_{11}H_1 + \mu_{12}H_2 + \mu_{13}H_3)(i,\hat{j},\hat{k}),$$
$$B_2(\hat{i},j,\hat{k}) = (\zeta_{21}E_1 + \zeta_{22}E_2 + \zeta_{23}E_3 + \mu_{21}H_1 + \mu_{22}H_2 + \mu_{23}H_3)(\hat{i},j,\hat{k}),$$
$$B_3(\hat{i},\hat{j},k) = (\zeta_{31}E_1 + \zeta_{32}E_2 + \zeta_{33}E_3 + \mu_{31}H_1 + \mu_{32}H_2 + \mu_{33}H_3)(\hat{i},\hat{j},k).$$

Denote $\mathcal{Z}_{pq}^{(\mathrm{f})}(\cdot) = \mathcal{S}_{pq}^{(\mathrm{f})}(\cdot,\zeta)$ and $\mathcal{M}_{pq}^{(\mathrm{f})}(\cdot) = \mathcal{S}_{pq}^{(\mathrm{f})}(\cdot,\mu)$, which are defined in (A.1), and $[\mathbf{h}_{fl}]_{l=1}^{4}$ are defined in (7). Combining the above results with the matrix form of the discrete single-curl operator, (B.1) can be recast into

$$\mathcal{C}(C_1,C_2,C_3)\mathbf{e}_{e1}$$
$$= \imath\omega(\left[\mathcal{Z}_{11}^{(\mathrm{f})} \quad \mathcal{Z}_{12}^{(\mathrm{f})} \quad \mathcal{Z}_{13}^{(\mathrm{f})} \quad \mathcal{Z}_{14}^{(\mathrm{f})}\right]\mathbf{e}_f$$
$$+ \left[\mathcal{M}_{11}^{(\mathrm{f})} \quad \mathcal{M}_{12}^{(\mathrm{f})} \quad \mathcal{M}_{13}^{(\mathrm{f})} \quad \mathcal{M}_{14}^{(\mathrm{f})}\right]\mathbf{h}_f). \quad \text{(B.2)}$$

B.2. Matrix representation of $\nabla\times\boldsymbol{H} = -\imath\omega\boldsymbol{D}$ at midpoints of edges

In this subsection, we discretize (1b) on subgrids 1, 2, 3 and 4 illustrated in Figs. 1(b), 1(c), 1(d), and 1(e), respectively. Similarly, we recast all formulas for each subgrid into matrix–vector form.

Using the FD discretization for (1b) at

- $(\hat{i},j,k)$, $(i,\hat{j},k)$ and $(i,j,\hat{k})$, respectively, in Subgrid 1 (Fig. 1(b));
- $(i,\hat{j},k)$, $(\hat{i},j,k)$ and $(\hat{i},\hat{j},\hat{k})$, respectively, in Subgrid 2 (Fig. 1(c));
- $(i,j,\hat{k})$, $(\hat{i},\hat{j},\hat{k})$ and $(\hat{i},j,k)$, respectively, in Subgrid 3 (Fig. 1(d));
- $(\hat{i},\hat{j},\hat{k})$, $(i,j,\hat{k})$ and $(i,\hat{j},k)$, respectively, in Subgrid 4 (Fig. 1(e)),

the resulting matrix representations are

$$\mathcal{C}(C_1,C_2,C_3)^*\mathbf{h}_{f1}$$
$$= -\imath\omega\left(\left[\mathcal{E}_{11}^{(\mathrm{e})} \quad \mathcal{E}_{12}^{(\mathrm{e})} \quad \mathcal{E}_{13}^{(\mathrm{e})} \quad \mathcal{E}_{14}^{(\mathrm{e})}\right]\mathbf{e}_e + \left[\mathcal{X}_{11}^{(\mathrm{e})} \quad \mathcal{X}_{12}^{(\mathrm{e})} \quad \mathcal{X}_{13}^{(\mathrm{e})} \quad \mathcal{X}_{14}^{(\mathrm{e})}\right]\mathbf{h}_e\right), \quad \text{(B.3a)}$$

$$\mathcal{C}(-C_1^*,-C_2^*,C_3)^*\mathbf{h}_{f2}$$
$$= -\imath\omega\left(\left[\mathcal{E}_{21}^{(\mathrm{e})} \quad \mathcal{E}_{22}^{(\mathrm{e})} \quad \mathcal{E}_{23}^{(\mathrm{e})} \quad \mathcal{E}_{24}^{(\mathrm{e})}\right]\mathbf{e}_e + \left[\mathcal{X}_{21}^{(\mathrm{e})} \quad \mathcal{X}_{22}^{(\mathrm{e})} \quad \mathcal{X}_{23}^{(\mathrm{e})} \quad \mathcal{X}_{24}^{(\mathrm{e})}\right]\mathbf{h}_e\right), \quad \text{(B.3b)}$$

$$\mathcal{C}(-C_1^*,C_2,-C_3^*)^*\mathbf{h}_{f3}$$
$$= -\imath\omega\left(\left[\mathcal{E}_{31}^{(\mathrm{e})} \quad \mathcal{E}_{32}^{(\mathrm{e})} \quad \mathcal{E}_{33}^{(\mathrm{e})} \quad \mathcal{E}_{34}^{(\mathrm{e})}\right]\mathbf{e}_e + \left[\mathcal{X}_{31}^{(\mathrm{e})} \quad \mathcal{X}_{32}^{(\mathrm{e})} \quad \mathcal{X}_{33}^{(\mathrm{e})} \quad \mathcal{X}_{34}^{(\mathrm{e})}\right]\mathbf{h}_e\right), \quad \text{(B.3c)}$$

$$\begin{aligned}&\mathcal{C}(C_1, -C_2^*, -C_3^*)^*\mathbf{h}_{f4}\\&= -\imath\omega\left(\begin{bmatrix}\mathcal{E}_{41}^{(\mathrm{e})} & \mathcal{E}_{42}^{(\mathrm{e})} & \mathcal{E}_{43}^{(\mathrm{e})} & \mathcal{E}_{44}^{(\mathrm{e})}\end{bmatrix}\mathbf{e}_e\right.\\&\quad\left.+\begin{bmatrix}\mathcal{X}_{41}^{(\mathrm{e})} & \mathcal{X}_{42}^{(\mathrm{e})} & \mathcal{X}_{43}^{(\mathrm{e})} & \mathcal{X}_{44}^{(\mathrm{e})}\end{bmatrix}\mathbf{h}_e\right), \qquad \text{(B.3d)}\end{aligned}$$

respectively.

B.3. Matrix representation of $\nabla \times \boldsymbol{H} = -\imath\omega\boldsymbol{D}$ at face centers

In this subsection, we discretize (1b) on subgrids 1, 2, 3 and 4 illustrated in Figs. 1(b), 1(c), 1(d), and 1(e), respectively. Similarly, we recast all formulas for each subgrid into matrix–vector form.

Using the FD discretization for (1b) at

- $(i, \hat{j}, \hat{k})$, $(\hat{i}, j, \hat{k})$ and $(\hat{i}, \hat{j}, k)$, respectively, in Subgrid 1 (Fig. 1(b));
- $(\hat{i}, j, \hat{k})$, $(i, \hat{j}, \hat{k})$ and (i, j, k), respectively, in Subgrid 2 (Fig. 1(c));
- $(\hat{i}, \hat{j}, k)$, (i, j, k) and $(i, \hat{j}, \hat{k})$, respectively, in Subgrid 3 (Fig. 1(d));
- (i, j, k), $(\hat{i}, \hat{j}, k)$ and $(\hat{i}, j, \hat{k})$, respectively, in Subgrid 4 (Fig. 1(e)),

the resulting matrix representations are

$$\begin{aligned}&\mathcal{C}(C_1, C_2, C_3)\mathbf{h}_{e1}\\&= -\imath\omega\left(\begin{bmatrix}\mathcal{E}_{11}^{(\mathrm{f})} & \mathcal{E}_{12}^{(\mathrm{f})} & \mathcal{E}_{13}^{(\mathrm{f})} & \mathcal{E}_{14}^{(\mathrm{f})}\end{bmatrix}\mathbf{e}_f\right.\\&\quad\left.+\begin{bmatrix}\mathcal{X}_{11}^{(\mathrm{f})} & \mathcal{X}_{12}^{(\mathrm{f})} & \mathcal{X}_{13}^{(\mathrm{f})} & \mathcal{X}_{14}^{(\mathrm{f})}\end{bmatrix}\mathbf{h}_f\right), \qquad \text{(B.4a)}\\&\mathcal{C}(-C_1^*, -C_2^*, C_3)\mathbf{h}_{e2}\\&= -\imath\omega\left(\begin{bmatrix}\mathcal{E}_{21}^{(\mathrm{f})} & \mathcal{E}_{22}^{(\mathrm{f})} & \mathcal{E}_{23}^{(\mathrm{f})} & \mathcal{E}_{24}^{(\mathrm{f})}\end{bmatrix}\mathbf{e}_f\right.\\&\quad\left.+\begin{bmatrix}\mathcal{X}_{21}^{(\mathrm{f})} & \mathcal{X}_{22}^{(\mathrm{f})} & \mathcal{X}_{23}^{(\mathrm{f})} & \mathcal{X}_{24}^{(\mathrm{f})}\end{bmatrix}\mathbf{h}_f\right), \qquad \text{(B.4b)}\\&\mathcal{C}(-C_1^*, C_2, -C_3^*)\mathbf{h}_{e3}\\&= -\imath\omega\left(\begin{bmatrix}\mathcal{E}_{31}^{(\mathrm{f})} & \mathcal{E}_{32}^{(\mathrm{f})} & \mathcal{E}_{33}^{(\mathrm{f})} & \mathcal{E}_{34}^{(\mathrm{f})}\end{bmatrix}\mathbf{e}_f\right.\\&\quad\left.+\begin{bmatrix}\mathcal{X}_{31}^{(\mathrm{f})} & \mathcal{X}_{32}^{(\mathrm{f})} & \mathcal{X}_{33}^{(\mathrm{f})} & \mathcal{X}_{34}^{(\mathrm{f})}\end{bmatrix}\mathbf{h}_f\right), \qquad \text{(B.4c)}\\&\mathcal{C}(C_1, -C_2^*, -C_3^*)\mathbf{h}_{e4}\\&= -\imath\omega\left(\begin{bmatrix}\mathcal{E}_{41}^{(\mathrm{f})} & \mathcal{E}_{42}^{(\mathrm{f})} & \mathcal{E}_{43}^{(\mathrm{f})} & \mathcal{E}_{44}^{(\mathrm{f})}\end{bmatrix}\mathbf{e}_f\right.\\&\quad\left.+\begin{bmatrix}\mathcal{X}_{41}^{(\mathrm{f})} & \mathcal{X}_{42}^{(\mathrm{f})} & \mathcal{X}_{43}^{(\mathrm{f})} & \mathcal{X}_{44}^{(\mathrm{f})}\end{bmatrix}\mathbf{h}_f\right), \qquad \text{(B.4d)}\end{aligned}$$

respectively.

Appendix C. Proofs for some theorems

C.1. Proof for Theorem 1

Proof. Let $\Pi = [\Pi_{pq}]_{p,q=1}^4 \in \mathbb{R}^{12n\times 12n}$ with $\Pi_{pp} = I_n \oplus 0_n \oplus 0_n$, for $p = 1, \ldots, 4$, $\Pi_{12} = \Pi_{21} = \Pi_{34} = \Pi_{43} = 0_n \oplus I_n \oplus 0_n$, $\Pi_{13} = \Pi_{31} = \Pi_{24} = \Pi_{42} = 0_n \oplus 0_n \oplus I_n$, $\Pi_{14} = \Pi_{41} = \Pi_{23} = \Pi_{32} = 0_{3n}$. Then we have

$$\Pi^\top \mathcal{S}^{(\mathrm{C})}(s)\Pi = \mathrm{diag}\left(S_1^{(\mathrm{C})}(s), S_2^{(\mathrm{C})}(s), S_3^{(\mathrm{C})}(s), S_4^{(\mathrm{C})}(s)\right) \qquad \text{(C.1a)}$$

with

$$S_1^{(\mathrm{C})}(s) = [S_{pq}^{(\mathrm{C})}(x,s)]_{p,q=1}^3, \quad S_2^{(\mathrm{C})}(s) = [S_{pq}^{(\mathrm{C})}(y,s)]_{p,q=1}^3, \qquad \text{(C.1b)}$$

$$S_3^{(\mathrm{C})}(s) = [S_{pq}^{(\mathrm{C})}(z,s)]_{p,q=1}^3, \quad S_4^{(\mathrm{C})}(s) = [S_{pq}^{(\mathrm{C})}(s)]_{p,q=1}^3, \qquad \text{(C.1c)}$$

which implies that $\mathcal{S}^{(\mathrm{C})}(s)$ is HPD. □

C.2. Proof of Theorem 4

Proof. From (19), it holds that

$$L^*L = \ell_q I_3 - \begin{bmatrix}\ell_1\\ \ell_2\\ \ell_3\end{bmatrix}\begin{bmatrix}\bar{\ell}_1 & \bar{\ell}_2 & \bar{\ell}_3\end{bmatrix},$$

$$LL^* = \ell_q I_3 - \begin{bmatrix}\bar{\ell}_1\\ \bar{\ell}_2\\ \bar{\ell}_3\end{bmatrix}\begin{bmatrix}\ell_1 & \ell_2 & \ell_3\end{bmatrix}.$$

It is easy to see that both L^*L and LL^* have eigenvalues 0, ℓ_q and ℓ_q. Moreover, $\mathbf{v}_0$ and $\bar{\mathbf{v}}_0$ are the eigenvectors of L^*L and LL^*, respectively, corresponding to zero eigenvalue. Since $\mathbf{v}_1$ and $\mathbf{v}_2$ satisfy $\begin{bmatrix}\bar{\ell}_1 & \bar{\ell}_2 & \bar{\ell}_3\end{bmatrix}\mathbf{v}_1 = 0$ and $\begin{bmatrix}\bar{\ell}_1 & \bar{\ell}_2 & \bar{\ell}_3\end{bmatrix}\mathbf{v}_2 = 0$, $\{\mathbf{v}_1, \ \mathbf{v}_2\}$ and $\{\bar{\mathbf{v}}_1, \ \bar{\mathbf{v}}_2\}$ are the eigenvectors of L^*L and LL^*, respectively, corresponding to eigenvalues ℓ_q, ℓ_q. By the definitions of $\mathbf{v}_i$, $i = 0, 1, 2$, we have $\mathbf{v}_i^*\mathbf{v}_j = 0$ for $i \neq j$ and $\|\mathbf{v}_2\|_2 = \|\mathbf{v}_0\|_2\|\mathbf{v}_1\|_2 = \sqrt{\ell_q}\|\mathbf{v}_1\|_2$. This implies that U and V are unitary, and L^*L and LL^* have eigendecompositions in (20).

Rewrite $\mathbf{v}_1$ and $\mathbf{v}_2$ as

$$\mathbf{v}_1 = \begin{bmatrix}\beta\bar{\ell}_3 - \bar{\ell}_2\\ \bar{\ell}_1 - \alpha\bar{\ell}_3\\ \alpha\bar{\ell}_2 - \beta\bar{\ell}_1\end{bmatrix} = L^*\mathbf{w} = -\bar{L}\mathbf{w},$$

$$\begin{aligned}\mathbf{v}_2 = \bar{\mathbf{v}}_0 \times \bar{\mathbf{v}}_1 &= \begin{bmatrix}(\alpha\ell_2 - \beta\ell_1)\bar{\ell}_2 - (\ell_1 - \alpha\ell_3)\bar{\ell}_3\\ (\beta\ell_3 - \ell_2)\bar{\ell}_3 - (\alpha\ell_2 - \beta\ell_1)\bar{\ell}_1\\ (\ell_1 - \alpha\ell_3)\bar{\ell}_1 - (\beta\ell_3 - \ell_2)\bar{\ell}_2\end{bmatrix}\\&= (\ell_q I - \mathbf{v}_0\mathbf{v}_0^*)\mathbf{w},\end{aligned}$$

where $\mathbf{w} = \begin{bmatrix}\alpha & \beta & 1\end{bmatrix}^\top$. Then, we have

$$\begin{aligned}&(\bar{\mathbf{v}}_1)^*L\mathbf{v}_1 = -\mathbf{w}^*L^*L\mathbf{v}_1 = -\ell_q\mathbf{w}^*\mathbf{v}_1 = 0,\\&(\bar{\mathbf{v}}_2)^*L\mathbf{v}_2 = \mathbf{w}^*(\ell_q I - \bar{\mathbf{v}}_0\mathbf{v}_0^\top)L(\ell_q I - \mathbf{v}_0\mathbf{v}_0^*)\mathbf{w} = \ell_q^2\mathbf{w}^*L\mathbf{w} = \ell_q^2\mathbf{v}_1^*\mathbf{w}\\&\qquad = 0,\\&(\bar{\mathbf{v}}_1)^*L\mathbf{v}_2 = (\bar{\mathbf{v}}_1)^*L(\ell_q I - \mathbf{v}_0\mathbf{v}_0^*)\mathbf{w} = \ell_q(\bar{\mathbf{v}}_1)^*L\mathbf{w} = -\ell_q(\bar{\mathbf{v}}_1)^*\bar{\mathbf{v}}_1\\&\qquad = -\ell_q\|\mathbf{v}_1\|_2^2,\\&(\bar{\mathbf{v}}_2)^*L\mathbf{v}_1 = \mathbf{w}^*(\ell_q I - \bar{\mathbf{v}}_0\bar{\mathbf{v}}_0^*)L\mathbf{v}_1 = \ell_q\mathbf{w}^*L\mathbf{v}_1 = \ell_q\mathbf{v}_1^*\mathbf{v}_1 = \ell_q\|\mathbf{v}_1\|_2^2.\end{aligned}$$

This implies the SVD of L in (21). □

C.3. Proof for Theorem 6

Proof. Define $\tilde{\mathbf{y}}_r = [\tilde{\mathbf{y}}_{r1}^*, \ \tilde{\mathbf{y}}_{r2}^*]^*$. From (25), we have

$$B^{-1}A_{(\mathrm{e})}B^{-1}A_{(\mathrm{f})}\tilde{\mathbf{y}}_{r1} = -\omega^2\tilde{\mathbf{y}}_{r1},$$

which implies that if ω is an eigenvalue of (24a), then $-\omega$ is also an eigenvalue. Let $\hat{\mathbf{y}}_r = \begin{bmatrix}B & 0\\ 0 & I\end{bmatrix}\tilde{\mathbf{y}}_r$. Then, (25) can be rewritten as

$$\begin{bmatrix}0 & -\imath A_{(\mathrm{e})}\\ -\imath B^{-1}A_{(\mathrm{f})}B^{-1} & 0\end{bmatrix}\hat{\mathbf{y}}_r = \omega\hat{\mathbf{y}}_r. \qquad \text{(C.2)}$$

The matrix in (C.2) forms a complex skew-Hamiltonian matrix. It follows that if ω is an eigenvalue of (C.2), then $\bar{\omega}$ is also an eigenvalue of (C.2). Therefore, (25) has eigenvalues ω, $-\omega$, $\bar{\omega}$ and $-\bar{\omega}$. □

Appendix D. Mathematical derivation of (25)

Since

$$\mathcal{M}^{-1}\mathcal{Z}\Phi^{-1} = \begin{bmatrix} \mathcal{M}_{(f)}^{-1} & 0 \\ 0 & \mathcal{M}_{(e)}^{-1} \end{bmatrix} \begin{bmatrix} 0 & \mathcal{Z}_{(f)} \\ \mathcal{Z}_{(e)} & 0 \end{bmatrix} \begin{bmatrix} \Phi_{(e)}^{-1} & 0 \\ 0 & \Phi_{(f)}^{-1} \end{bmatrix} = \begin{bmatrix} 0 & \mathcal{M}_{(f)}^{-1}\mathcal{Z}_{(f)}\Phi_{(f)}^{-1} \\ \mathcal{M}_{(e)}^{-1}\mathcal{Z}_{(e)}\Phi_{(e)}^{-1} & 0 \end{bmatrix},$$

$$\Phi^{-1}\mathcal{X}\mathcal{M}^{-1} = \begin{bmatrix} \Phi_{(e)}^{-1} & 0 \\ 0 & \Phi_{(f)}^{-1} \end{bmatrix} \begin{bmatrix} 0 & \mathcal{X}_{(e)} \\ \mathcal{X}_{(f)} & 0 \end{bmatrix} \begin{bmatrix} \mathcal{M}_{(f)}^{-1} & 0 \\ 0 & \mathcal{M}_{(e)}^{-1} \end{bmatrix} = \begin{bmatrix} 0 & \Phi_{(e)}^{-1}\mathcal{X}_{(e)}\mathcal{M}_{(e)}^{-1} \\ \Phi_{(f)}^{-1}\mathcal{X}_{(f)}\mathcal{M}_{(f)}^{-1} & 0 \end{bmatrix}$$

and

$$\begin{aligned} &\mathcal{M}^{-1} + \mathcal{M}^{-1}\mathcal{Z}\Phi^{-1}\mathcal{X}\mathcal{M}^{-1} \\ &= \mathcal{M}^{-1} + \mathcal{M}^{-1} \begin{bmatrix} 0 & \mathcal{Z}_{(f)} \\ \mathcal{Z}_{(e)} & 0 \end{bmatrix} \begin{bmatrix} \Phi_{(e)}^{-1} & 0 \\ 0 & \Phi_{(f)}^{-1} \end{bmatrix} \begin{bmatrix} 0 & \mathcal{X}_{(e)} \\ \mathcal{X}_{(f)} & 0 \end{bmatrix} \mathcal{M}^{-1} \\ &= \operatorname{diag}\left(\mathcal{F}_{(f)}, \mathcal{F}_{(e)}\right) \end{aligned}$$

with

$$\mathcal{F}_{(c)} = \mathcal{M}_{(c)}^{-1} + \mathcal{M}_{(c)}^{-1}\mathcal{Z}_{(c)}\Phi_{(c)}^{-1}\mathcal{X}_{(c)}\mathcal{M}_{(c)}^{-1}, \quad c = \text{e or f},$$

the product of matrices in (24b) can be reformulated as

$$\begin{aligned} &\begin{bmatrix} \mathcal{M}^{-1}\mathcal{Z} & -I_{24n} \\ I_{24n} & 0 \end{bmatrix} \begin{bmatrix} \Phi^{-1} & 0 \\ 0 & \mathcal{M}^{-1} \end{bmatrix} \begin{bmatrix} \mathcal{X}\mathcal{M}^{-1} & I_{24n} \\ -I_{24n} & 0 \end{bmatrix} \\ &= \begin{bmatrix} (\mathcal{M}^{-1} + \mathcal{M}^{-1}\mathcal{Z}\Phi^{-1}\mathcal{X}\mathcal{M}^{-1}) & \mathcal{M}^{-1}\mathcal{Z}\Phi^{-1} \\ \Phi^{-1}\mathcal{X}\mathcal{M}^{-1} & \Phi^{-1} \end{bmatrix} \\ &= \left[\begin{array}{cc|cc} \mathcal{F}_{(f)} & 0 & 0 & \mathcal{M}_{(f)}^{-1}\mathcal{Z}_{(f)}\Phi_{(f)}^{-1} \\ 0 & \mathcal{F}_{(e)} & \mathcal{M}_{(e)}^{-1}\mathcal{Z}_{(e)}\Phi_{(e)}^{-1} & 0 \\ \hline 0 & \Phi_{(e)}^{-1}\mathcal{X}_{(e)}\mathcal{M}_{(e)}^{-1} & \Phi_{(e)}^{-1} & 0 \\ \Phi_{(f)}^{-1}\mathcal{X}_{(f)}\mathcal{M}_{(f)}^{-1} & 0 & 0 & \Phi_{(f)}^{-1} \end{array}\right]. \end{aligned}$$

This implies that

$$\begin{aligned} &\Pi_1 \begin{bmatrix} \mathcal{M}^{-1}\mathcal{Z} & -I_{24n} \\ I_{24n} & 0 \end{bmatrix} \begin{bmatrix} \Phi^{-1} & 0 \\ 0 & \mathcal{M}^{-1} \end{bmatrix} \begin{bmatrix} \mathcal{X}\mathcal{M}^{-1} & I_{24n} \\ -I_{24n} & 0 \end{bmatrix} \Pi_1^\top \\ &= \operatorname{diag}\left(\begin{bmatrix} \mathcal{F}_{(f)} & \mathcal{M}_{(f)}^{-1}\mathcal{Z}_{(f)}\Phi_{(f)}^{-1} \\ \Phi_{(f)}^{-1}\mathcal{X}_{(f)}\mathcal{M}_{(f)}^{-1} & \Phi_{(f)}^{-1} \end{bmatrix}, \begin{bmatrix} \mathcal{F}_{(e)} & \mathcal{M}_{(e)}^{-1}\mathcal{Z}_{(e)}\Phi_{(e)}^{-1} \\ \Phi_{(e)}^{-1}\mathcal{X}_{(e)}\mathcal{M}_{(e)}^{-1} & \Phi_{(e)}^{-1} \end{bmatrix} \right), \end{aligned} \tag{D.1}$$

where $\Pi_1 = [\mathbf{e}_1, \mathbf{e}_3, \mathbf{e}_4, \mathbf{e}_2]_{4\times 4} \otimes I_{12n} \in \mathbb{R}^{48n\times 48n}$. Let $\Pi_2 = [\mathbf{e}_1, \mathbf{e}_3, \mathbf{e}_4, \mathbf{e}_2]_{4\times 4} \otimes I_{8n} \in \mathbb{R}^{32n\times 32n}$. Then

$$\begin{aligned} \Pi_1 \operatorname{diag}(\mathcal{P}_r, \mathcal{Q}_r)\, \Pi_2^\top &= \Pi_1 \operatorname{diag}(P_r, Q_r, Q_r, P_r)\, \Pi_2^\top \\ &= \operatorname{diag}(P_r, P_r, Q_r, Q_r) \end{aligned} \tag{D.2a}$$

and

$$\Pi_2 \begin{bmatrix} 0 & I_2 \otimes \Sigma_r^{-1} \\ -I_2 \otimes \Sigma_r^{-1} & 0 \end{bmatrix} \Pi_2^\top = \begin{bmatrix} 0 & 0 & 0 & \Sigma_r^{-1} \\ 0 & 0 & -\Sigma_r^{-1} & 0 \\ 0 & \Sigma_r^{-1} & 0 & 0 \\ -\Sigma_r^{-1} & 0 & 0 & 0 \end{bmatrix}. \tag{D.2b}$$

Substituting (D.1) and (D.2) into (24), we obtain (25).

References

[1] R.-L. Chern, H.-E. Hsieh, T.-M. Huang, W.-W. Lin, W. Wang, SIAM J. Matrix Anal. Appl. 36 (2015) 203–224.
[2] T.-M. Huang, T. Li, R.-L. Chern, W.-W. Lin, J. Comput. Phys. 379 (2019) 118–131.
[3] C. Kittel, Introduction to Solid State Physics, Wiley, New York, NY, 2005.
[4] K.M. Ho, C.T. Chan, C.M. Soukoulis, Phys. Rev. Lett. 65 (25) (1990) 3152.
[5] S.G. Johnson, J.D. Joannopoulos, Opt. Express 8 (3) (2001) 173–190.
[6] Z. Chen, Q. Du, J. Zou, SIAM J. Numer. Anal. 37 (2000) 1542–1570.
[7] D.C. Dobson, J. Pasciak, Comput. Methods Appl. Math. 1 (2001) 138–153.
[8] J. Jin, The Finite Element Method in Electromagnetics, John Wiley, New York, NY, 2002.
[9] J.-C. Nédélec, Numer. Math. 50 (1) (1986) 57–81.
[10] R.L. Chern, C.C. Chang, Chien-C. Chang, R.R. Hwang, Phys. Rev. E 68 (2003) 26704.
[11] T.-M. Huang, H.-E. Hsieh, W.-W. Lin, W. Wang, SIAM J. Matrix Anal. Appl. 34 (2013) 369–391.
[12] T.-M. Huang, H.-E. Hsieh, W.-W. Lin, W. Wang, Math. Comput. Model. 58 (2013) 379–392.
[13] F. Xu, Y. Zhang, W. Hong, K. Wu, T.-J. Cui, IEEE Trans. Microw. Theory Tech. 51 (11) (2003) 2221–2227.
[14] K. Yee, IEEE Trans. Antennas and Propagation 14 (1966) 302–307.
[15] S. Davydycheva, V. Druskin, in: M. Oristaglio, B. Spies (Eds.), Three-DImensional Electromagnetics, Society of Exploration Geophysicists, 1999, pp. 138–145.
[16] S. Davydycheva, V. Druskin, T. Habashy, Geophysics 68 (5) (2003) 1525–1536.
[17] P. Jaysaval, D.V. Shantsev, S. de la Kethulle de Ryhove, T. Bratteland, Geophys. J. Int. 207 (2016) 1554–1572.
[18] E. Alkan, V. Demir, A. Elsherbeni, E. Arvas, IEEE Trans. Antennas and Propagation 58 (3) (2010) 817–823.
[19] E. Alkan, V. Demir, A. Elsherbeni, E. Arvas, Double-Grid Finite-Difference Frequency-Domain (DG-FDFD) Method for Scattering from Chiral Objects, in: Synthesis Lectures on Computational Electromagnetics, vol. 8, Morgan & Claypool Publishers LLC, 2013.
[20] M.J. Mehl, D. Hicks, C. Toher, O. Levy, R.M. Hanson, G. Hart, S. Curtarolo, Comput. Mater. Sci. 136 (2017) S1–S828.
[21] T.-M. Huang, T. Li, W.-D. Li, J.-W. Lin, W.-W. Lin, H. Tian, Solving Three Dimensional Maxwell Eigenvalue Problem with Fourteen Bravais Lattices, Technical Report, 2018, arXiv:1806.10782.
[22] T.-M. Huang, W.-W. Lin, H. Tsai, W. Wang, Comput. Phys. Comm. 245 (2019) 106841.
[23] Z. Jia, C. Li, Sci. China Math. 57 (2014) 1733–1752.
[24] C.-R. Lee, Residual Arnoldi Method: Theory, Package and Experiments (Ph.D. thesis), Department of Computer Science, University of Maryland at College Park, 2007, TR-4515.
[25] W.R. Ferng, W.-W. Lin, C.-S. Wang, Comput. Math. Appl. 33 (1997) 23–40.